Strength and Deformation Characteristics of Sand–Rubber Mixtures under Torsional Shear Loadings

Shao-Heng He, Ph.D.[1]; Zhen-Yu Yin, Ph.D.[2]; Zhi Ding, Ph.D.[3]; and Rui-Dong Li[4]

Abstract: Granulated sand–rubber mixtures have been widely employed in ground improvement. Previous studies have extensively investigated the mechanical behavior of such geomaterials under conventional triaxial conditions, but little is known about the influence of varying principal stress directions (α_σ) on their strength and deformation characteristics. To address this gap, drained hollow cylinder torsional shear tests were conducted, including monotonic tests with different α_σ values and cyclic tests involving cyclic principal stress rotation (CPSR), on Fujian sand mixed with granulated rubber in six different mass ratios. The test results reveal that the inclusion of granulated rubber has a significant impact on the variation of peak strength with respect to α_σ. As the rubber content (R_c) increases, the strength anisotropy of the mixture reduces, and the strength failure surface in the $(\sigma_z\text{-}\sigma_\theta)/2\text{–}\tau_{z\theta}$ plane transitions from a circular to an elliptical shape with a noticeably reduced radius in the $\tau_{z\theta}$-axis direction. A formulation was proposed to characterize the strength envelope of sand–rubber mixtures. The inclusion of granulated rubber promotes the contractive behavior of the mixture. Under CPSR cyclic loading, higher rubber content leads to an increase in various strain components. The addition of rubber particles was observed to reduce the mixture's noncoaxiality under CPSR, but this effect reduces at higher stress levels. **DOI: 10.1061/JGGEFK.GTENG-13008.**

Author keywords: Rubber–sand mixture; Hollow cylinder torsional shear; Granular material; Principal stress rotation.

Introduction

Recycled rubber granules with lightweight properties have been increasingly utilized in various geotechnical engineering applications, such as retaining wall, slope reinforcement, backfilling, and landfilling, due to their notable vibration reduction capabilities and contribution to a more sustainable world (Ari and Akbulut 2022; Fu et al. 2014; Pamukcu and Akbulut 2006; Qi et al. 2018). In these engineering practices, the inclination and rotation of principal stress axes in soil elements under external loads are common occurrences. For example, in slope engineering projects, the variation in the inclination angle of the major principal stress (α_σ) of soil elements across different regions of the slope, ranging from 0° to 90°, can significantly influence the strength characteristics and the critical failure surface (Gao and Zhao 2012). The marine backfilled foundations may exhibit plastic deformation due to the cyclic principal stress rotation induced by wave loading, potentially leading to structural tilting and posing risks to the stability of engineering structures. Hence, investigating the strength and deformation behavior of sand–rubber composites while considering the inclination and rotation of the principal stress axis holds paramount engineering significance.

The hollow cylinder apparatus (HCA) has proven to be a valuable tool for investigating the mechanical behavior of soils under varying major principal stress axes. Previous studies have conducted monotonic hollow cylinder torsional shear (HCTS) tests on granular materials at different α_σ values, revealing that as α_σ increases, the peak strength of sands initially decreases, reaching its minimum at $\alpha_\sigma = 60\text{–}75°$, before slightly increasing or stabilizing (Cai et al. 2018; Miura et al. 1986; Xiong et al. 2016). This strength anisotropy, marked by fluctuations in peak strength concerning the principal stress direction, is heavily influenced by the preferred particle orientation in relation to bedding planes and principal stress axes. Besides, the noncoaxiality between of the directions of the principal strain increment and their corresponding principal stress has been demonstrated to be an intrinsic property of soils (Gutierrez et al. 1991; Yang et al. 2007; Cai 2010). Noncoaxiality always occurs in soils when the principal stress is rotated due to three-dimensional (3D) loadings that the marine foundations typically endure in practical engineering. Incorporating noncoaxiality in flow rules is essential for developing more realistic and accurate constitutive models for soils, enabling the numerical analysis of strain localization and bifurcation in soils under various loading conditions (Feng and Zhang 2023; Shaverdi et al. 2014). By integrating the noncoaxial nonassociated flow rule into the revised 3D Mohr–Coulomb model, Huang et al. (2010) developed a noncoaxial constitutive model that accurately predicts the stress–strain relationship and the initiation of strain localization in sands. Furthermore, existing studies indicate that the degree of noncoaxiality tends to decrease with increasing stress levels, while remaining independent of the intermediate principal stress coefficient (Cai et al. 2013; Yu et al. 2016). This noncoaxiality between stress and strain increment is associated with the noncoaxiality between the current contact fabric and strain rates, or the distributions of interparticle contact and forces (Pouragha et al. 2021). However, to date, there have been few investigations into the HCTS tests on sand–rubber mixtures, resulting in a gap in understanding the specific

[1]Postdoc Fellow, Dept. of Civil and Environmental Engineering, Hong Kong Polytechnic Univ., No. 11 Yuk Choi Rd., Hung Hom, Kowloon, Hong Kong 999077, China. Email: heshaoheng@zju.edu.cn

[2]Professor, Dept. of Civil and Environmental Engineering, Hong Kong Polytechnic Univ., No. 11 Yuk Choi Rd., Hung Hom, Kowloon, Hong Kong 999077, China (corresponding author). Email: zhenyu.yin@polyu.edu.hk

[3]Professor, Dept. of Civil Engineering, Hangzhou City Univ., No. 48 Huzhou St., Hangzhou 310015, China. Email: dingz@hzcu.edu.cn

[4]Ph.D. Candidate, Dept. of Civil and Environmental Engineering, Hong Kong Polytechnic Univ., No. 11 Yuk Choi Rd., Hung Hom, Kowloon, Hong Kong 999077, China. Email: 22072096r@connect.polyu.hk

Note. This manuscript was submitted on May 10, 2024; approved on May 12, 2025; published online on August 20, 2025. Discussion period open until January 20, 2026; separate discussions must be submitted for individual papers. This paper is part of the ***Journal of Geotechnical and Geoenvironmental Engineering***, © ASCE, ISSN 1090-0241.

impacts of incorporating soft rubber particles on strength, deformation, and noncoaxiality behaviors under varying principal stress axis directions.

Previous studies have investigated how the properties of granulated rubber particles (such as shape, size, and content) impact the strength and deformation of sand–rubber mixtures, primarily through triaxial shear tests or direct shear tests. The existing studies extensively showcased the variations in shear strength depending on the mass ratio of rubber particles to sand particles, which are significantly influenced by the physical conditions (such as the shape and contact area) of particle contacts (Ari and Akbulut 2022, 2024; Dai et al. 2024; Fu et al. 2014, 2017; Kim and Santamarina 2008; Lee et al. 2014; Li et al. 2019; Mashiri et al. 2015). Most of the studies concluded that the presence of granulated rubber reduces the shear strength of the mixture, unlike tire chips, and adding rubber enhances the compressibility of the mixture (Asadi et al. 2018; Cheng et al. 2023; Dai et al. 2023; Wang et al. 2018). These studies suggest that factors such as interparticle sliding, grain rearrangement, and distortion, as well as the interlocking of individual rubber particles, play pivotal roles in the strength and deformation mechanisms of sand–rubber mixtures. While the mechanical properties of sand–rubber mixtures have been extensively explored through traditional triaxial and direct shear tests, the existing HCTS experiments on sand–rubber mixtures are limited in scope, focusing solely on the aspect of undrained strength or dynamic modulus (Ahmad and Fakharian 2020; Sarajpoor et al. 2020). The investigation of strength anisotropy in sand–rubber mixtures across different principal stress axis orientations and the impact of principal stress axis rotation on noncoaxiality behavior is rarely conducted using HCTS tests. The mechanical behavior of sand–rubber mixtures under intricate principal stress axis orientations remains unclear, possibly leading to inaccurate designs in practical engineering applications, underscoring the pressing need for further study in this domain.

The primary objective of this study is to assess the strength and deformation characteristics of sand–rubber mixtures under varying principal stress directions (α_σ). To achieve this goal, an extensive series of drained hollow cylinder torsional shear tests is carried out on Fujian sand mixed with granulated rubber in six different mass ratios. These tests include monotonic tests at various α_σ values and cyclic tests involving stress paths of pure principal stress rotation. This study, for the first time, to the best of our knowledge, elucidates the impact of granulated rubber content (R_c) on the shape of the mixture's failure surface in both generalized stress and $(\sigma_z\text{-}\sigma_\theta)/2$–$\tau_{z\theta}$ planes. An equation capable of characterizing the failure surface of sand–rubber mixtures is proposed. Furthermore, this study delves into the essential role of granulated rubber in dictating the deformation and noncoaxiality behavior of the mixture under cyclic principal stress rotation. The insights gained from this investigation shed light on the mechanical interplay between deformable rubber particles and principal stress direction, contributing to the optimization of design strategies for other deformable materials used in soil reinforcement.

Test Materials and Method

Test Materials

The host granular material utilized is Fujian sand (refer to Fig. 1), recognized as the standard sand in China. The particle shape indices and basic mechanical properties under HCTS tests of this sand can be found in He et al. (2024, 2025). The granular rubber utilized is obtained by shredding discarded tires, as shown in Fig. 1. The particle size distribution curves of the Fujian sand and granular rubber employed in this study are identical and depicted in Fig. 1, with the mean particle size (d_{50}) and the uniformity coefficient (C_u) clearly indicated. The uniform-sized sand and rubber particles were selected to partially mitigate the influence of particle gradation, thereby highlighting the fundamental impact of compressible rubber particles. The maximum size ratio of sand and rubber particles to the wall thickness of the hollow cylinder specimen is less than 1:10, which meets the requirements for conducting hollow cylinder torsional shear tests as specified by the Japanese Geotechnical Society Standards (2020). The specific gravity of Fujian sand is 2.65, while the specific gravity of the rubber is 1.1. This study investigated granulated sand–rubber mixtures with six different rubber contents (R_c), specifically $R_c = 0\%$ (i.e., clean sand), 5%, 10%, 20%, 40%, and 100% (i.e., clean rubber). Note that R_c represents the percentage of rubber mass in relation to the total mass, i.e., $R_c = m_r/(m_r + m_s)$, where m_r signifies the mass of rubber and m_s signifies the mass of Fujian sand. The Chinese code GB/T 50123–2019 is followed for the determination of maximum and minimum void ratios (e_{max} and e_{min}) of sand–rubber mixtures (Chinese Standard 2019). Table 1 and Fig. 2 depict the variation of e_{max} and e_{min} for the six sand–rubber mixtures in relation to different R_c values. Transitional rubber contents are observed around $R_c = 15\%$–20%. Beyond this threshold, there is a rapid increase in both e_{max} and e_{min} with increasing R_c, signifying the shift toward rubber

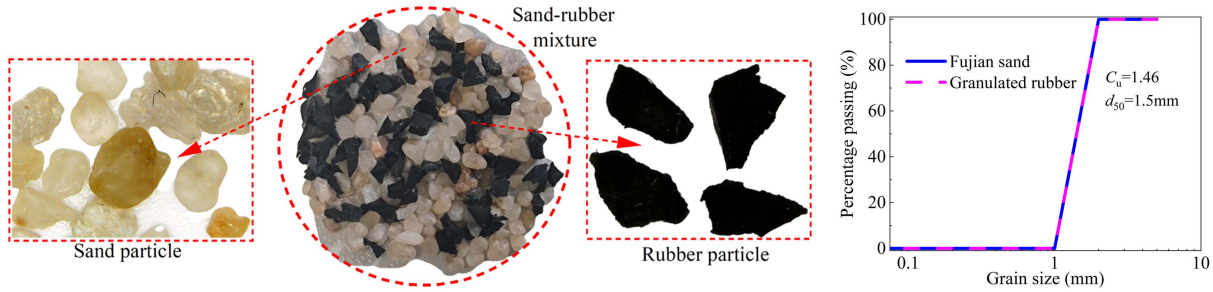

Fig. 1. Test materials and particle size distributions.

Table 1. Index void ratios for sand–rubber mixtures

Index void ratios	Sand with $R_c = 0\%$	Sand with $R_c = 5\%$	Sand with $R_c = 10\%$	Sand with $R_c = 20\%$	Sand with $R_c = 40\%$	Sand with $R_c = 100\%$
e_{min}	0.512	0.441	0.476	0.449	0.502	0.506
e_{max}	0.884	0.943	0.959	1.056	1.151	1.481

J. Geotech. Geoenviron. Eng., 2025, 151(11): 04025122

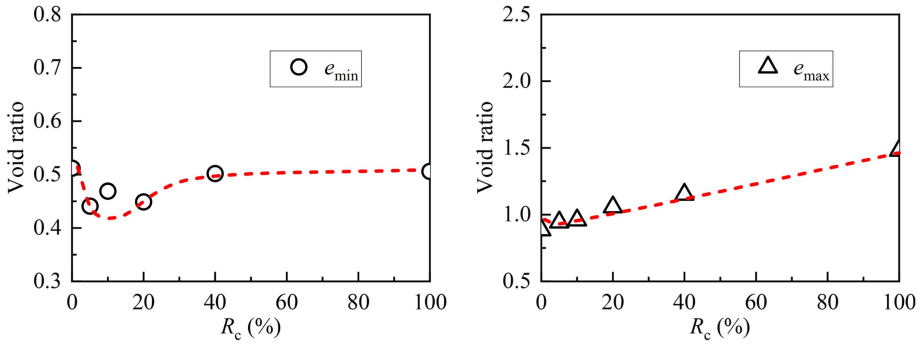

Fig. 2. e_{max} and e_{min} versus R_c.

particles taking on a predominant role in the packing structure. Rubber particles are primarily used as lightweight fill materials in geotechnical engineering and are typically in a compacted state after ground compaction. This study, therefore, concentrates on the behavior of dense sand–rubber mixtures. For all materials examined in this research, the initial relative density was set to 80%.

The initial fabric of the sand–rubber mixtures was captured through computed tomography (CT) scans. Each material was fabricated into cylindrical specimens measuring 2.45 cm in height and 5.2 cm in diameter using the same procedure employed in the HCTS tests. In Fig. 3, the CT scan images of the six materials are presented, which clearly demonstrate that the specimen preparation technique we utilized ensures a uniform distribution of the mixture.

Test Setup and Definitions

A HCA, similar to the design described by Cai et al. (2018), was utilized in this study. It integrates global measurement sensors and enables independent control of axial force (W), torque (T), back pressure, outer cell pressure (p_0), and inner cell pressure (p_i) [see Fig. 4(a)]. The equations for calculating stresses and strains experienced by the hollow cylinder soil element, including vertical (σ_z/ε_z), radial (σ_r/ε_r), circumferential ($\sigma_\theta/\varepsilon_\theta$), and torsional shear ($\tau_{z\theta}/\gamma_{z\theta}$), are provided in Table 2. This table also includes the relationships for major, intermediate, and minor principal stresses (σ_1, σ_2, and σ_3), strains (ε_1, ε_2, and ε_3), as well as stress–strain work-conjugate variables such as mean effective stress (p')–volumetric strain (ε_v) and deviatoric stress (q)–deviatoric strain (ε_q). The intermediate principal stress coefficient is defined as $b = (\sigma_2\text{-}\sigma_3)/(\sigma_1\text{-}\sigma_3)$

$$\alpha_\sigma = \frac{1}{2}\arctan\left(\frac{2\tau_{z\theta}}{\sigma_z - \sigma_\theta}\right) \tag{1}$$

$$\alpha_{d\varepsilon} = \frac{1}{2}\arctan\left(\frac{d\gamma_{z\theta}}{d\varepsilon_z - d\varepsilon_\theta}\right) \tag{2}$$

$$\beta = \alpha_{d\varepsilon} - \alpha_\sigma \tag{3}$$

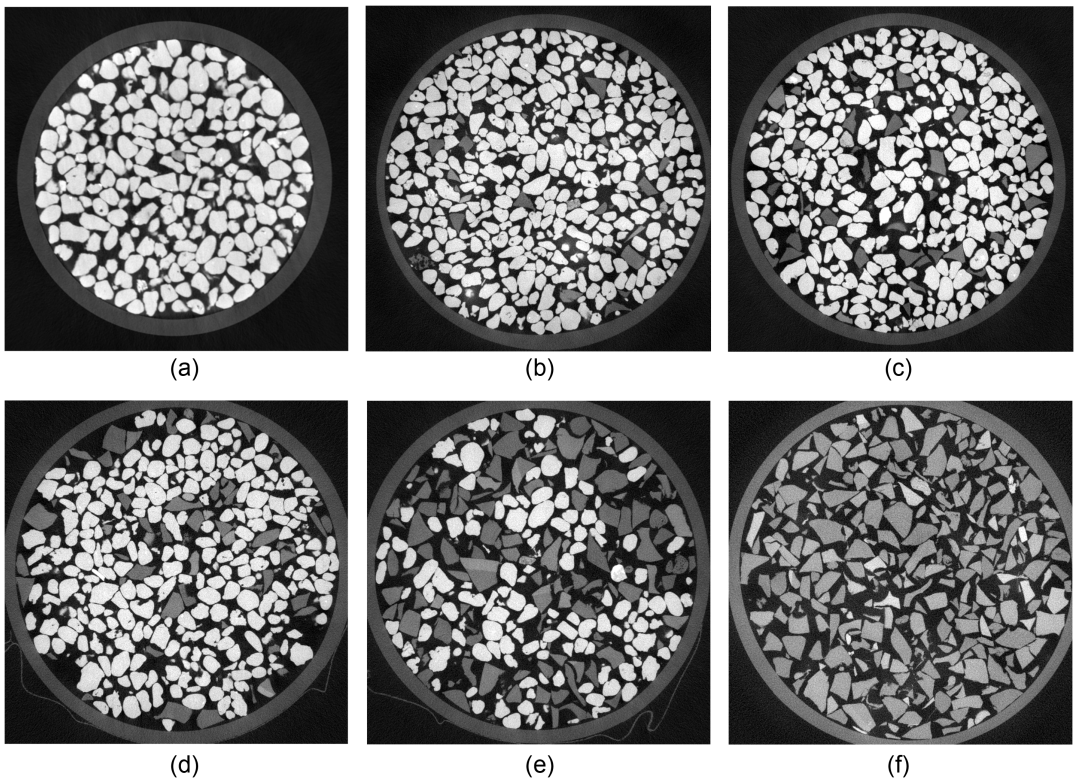

Fig. 3. CT images of mixtures: (a) $R_c = 0\%$; (b) $R_c = 5\%$; (c) $R_c = 10\%$; (d) $R_c = 20\%$; (e) $R_c = 40\%$; and (f) $R_c = 100\%$.

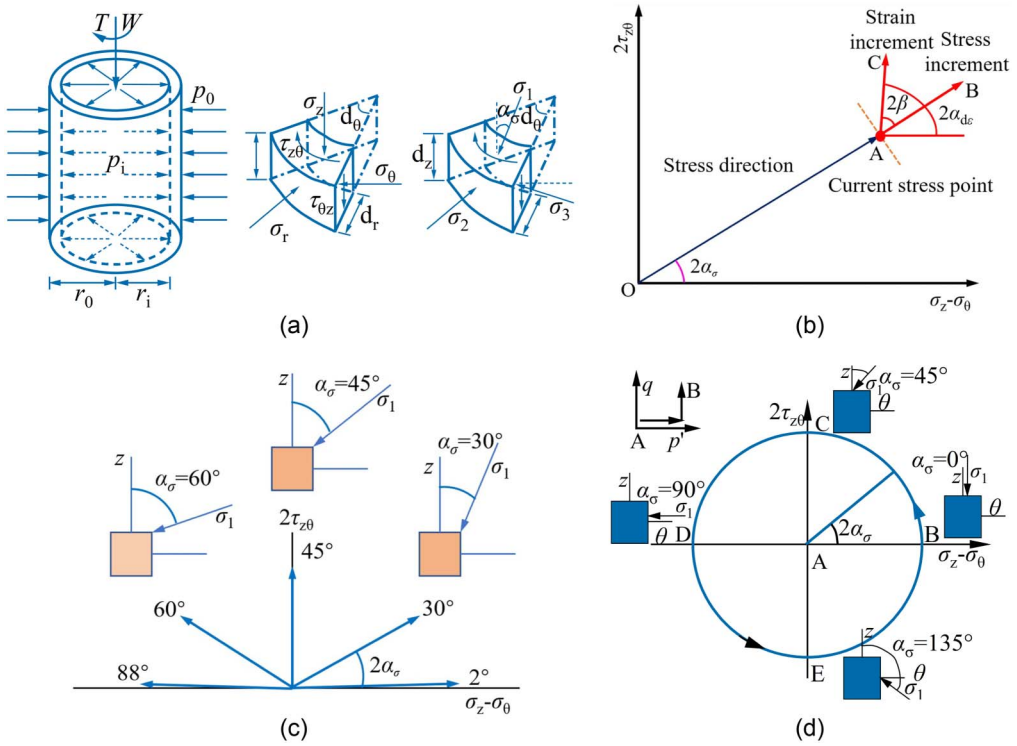

Fig. 4. Illustrations for test program: (a) stresses on a representative soil specimen's wall element; (b) definitions for noncoaxiality angle; (c) monotonic stress path; and (d) princial stress rotation stress path.

Table 2. Equations for calculating HCA stresses and strains

Component	Stress	Strain
Vertical	$\sigma_z = \frac{W}{\pi(r_0^2 - r_i^2)} + \frac{p_0 r_0^2 - p_i r_i^2}{r_0^2 - r_i^2}$	$\varepsilon_z = \frac{z}{H}$
Radial	$\sigma_r = \frac{p_0 r_0 + p_i r_i}{r_0 + r_i}$	$\varepsilon_r = -\frac{u_0 - u_i}{r_0 - r_i}$
Circumferential	$\sigma_\theta = \frac{p_0 r_0 - p_i r_i}{r_0 - r_i}$	$\varepsilon_\theta = -\frac{u_0 + u_i}{r_0 + r_i}$
Shear	$\tau_{z\theta} = \frac{3T}{2\pi(r_0^3 - r_i^3)}$	$\varepsilon_{z\theta} = \frac{2\theta(r_0^3 - r_i^3)}{3H(r_0^2 - r_i^2)}$
Major principal	$\sigma_1 = \frac{\sigma_z + \sigma_\theta}{2} + \sqrt{\left(\frac{\sigma_z - \sigma_\theta}{2}\right)^2 + \tau_{z\theta}^2}$	$\varepsilon_1 = \frac{\varepsilon_z + \varepsilon_\theta}{2} + \sqrt{\left(\frac{\varepsilon_z - \varepsilon_\theta}{2}\right)^2 + \left(\frac{\gamma_{z\theta}}{2}\right)^2}$
Intermediate principal	$\sigma_2 = \sigma_r$	$\varepsilon_2 = \varepsilon_r$
Minor principal	$\sigma_3 = \frac{\sigma_z + \sigma_\theta}{2} - \sqrt{\left(\frac{\sigma_z - \sigma_\theta}{2}\right)^2 + \tau_{z\theta}^2}$	$\varepsilon_3 = \frac{\varepsilon_z + \varepsilon_\theta}{2} - \sqrt{\left(\frac{\varepsilon_z - \varepsilon_\theta}{2}\right)^2 + \left(\frac{\gamma_{z\theta}}{2}\right)^2}$
Deviatoric	$q = \sqrt{\frac{1}{2}[(\sigma_1 - \sigma_2)^2 + (\sigma_2 - \sigma_3)^2 + (\sigma_3 - \sigma_1)^2]}$	$\varepsilon_q = \sqrt{\frac{2}{9}[(\varepsilon_1 - \varepsilon_2)^2 + (\varepsilon_2 - \varepsilon_3)^2 + (\varepsilon_3 - \varepsilon_1)^2]}$
Volumetric	$p' = \frac{\sigma_1 + \sigma_2 + \sigma_3}{3}$	$\varepsilon_v = \varepsilon_1 + \varepsilon_2 + \varepsilon_3$

In HCA loading conditions, the stress state point (A) is typically represented in the $[(\sigma_z\text{-}\sigma_\theta)/2, \tau_{z\theta}]$ stress plane [refer to Fig. 4(b)]. A vector (OA) originating from the axes' origin forms an angle of $2\alpha_\sigma$ from the $(\sigma_z\text{-}\sigma_\theta)/2$ axis [as shown in Fig. 4(b)], where α_σ is the angle of the major principal stress from the vertical z axis, according to Eq. (1). The angle $\alpha_{d\varepsilon}$ signifies the inclination of the major principal strain increment direction to the vertical z axis [Eq. (2)]. This representation [Fig. 4(b)] is particularly helpful as it immediately indicates the noncoaxiality, β, between the directions of principal axes of strain increment and stress by comparing α_σ and $\alpha_{d\varepsilon}$ [Eq. (3)].

Test Program

The hollow cylinder specimens have an inner diameter of 60 mm, an outer diameter of 100 mm, and a height of 200 mm. The dry tamping method was employed to fabricate the hollow cylindrical specimens. Rubber particles and sand particles are thoroughly mixed

Table 3. Test program for monotonic loading

Material	α_σ (°)	b	p' (kPa)	e_0
Sand with $R_c = 0\%$	2	0.5	100	0.563
	30	0.5	100	0.564
	45	0.5	100	0.562
	60	0.5	100	0.563
	88	0.5	100	0.565
Sand with $R_c = 5\%$	2	0.5	100	0.526
	30	0.5	100	0.526
	45	0.5	100	0.526
	60	0.5	100	0.526
	88	0.5	100	0.526
Sand with $R_c = 10\%$	2	0.5	100	0.551
	30	0.5	100	0.551
	45	0.5	100	0.553
	60	0.5	100	0.552
	88	0.5	100	0.553
Sand with $R_c = 20\%$	2	0.5	100	0.531
	30	0.5	100	0.533
	45	0.5	100	0.533
	60	0.5	100	0.528
	88	0.5	100	0.531
Sand with $R_c = 40\%$	2	0.5	100	0.547
	30	0.5	100	0.543
	45	0.5	100	0.549
	60	0.5	100	0.550
	88	0.5	100	0.552
Sand with $R_c = 100\%$	2	0.5	100	0.553
	30	0.5	100	0.556
	45	0.5	100	0.530
	60	0.5	100	0.530
	88	0.5	100	0.552

Table 4. Test program for CPSR loading

Material	$\sigma_1 - \sigma_3$ (kPa)	b	p' (kPa)	e_0
Sand with $R_c = 0\%$	30	0.5	100	0.573
	60	0	100	0.574
	60	0.5	100	0.569
	60	1	100	0.571
	80	0.5	100	0.571
Sand with $R_c = 5\%$	30	0.5	100	0.534
	60	0	100	0.530
	60	0.5	100	0.524
	60	1	100	0.522
	80	0.5	100	0.525
Sand with $R_c = 10\%$	30	0.5	100	0.548
	60	0	100	0.549
	60	0.5	100	0.550
	60	1	100	0.549
	80	0.5	100	0.547
Sand with $R_c = 20\%$	30	0.5	100	0.525
	60	0	100	0.527
	60	0.5	100	0.515
	60	1	100	0.515
	80	0.5	100	0.521
Sand with $R_c = 40\%$	30	0.5	100	0.533
	60	0	100	0.524
	60	0.5	100	0.536
	60	1	100	0.527
	80	0.5	100	0.530

and visually inspected during the specimen preparation process to ensure a homogeneous blend. The specimen is saturated by flushing it with carbon dioxide and deaired water, followed by back pressure saturation to ensure a B value exceeding 0.95.

To investigate the strength mechanisms of sand–rubber mixtures under varying α_σ values, drained monotonic tests were carried out on six different sand–rubber compositions. The tests involved increasing q monotonically while keeping α_σ fixed at 2°, 30°, 45°, 60°, and 88° [refer to Fig. 4(c)]. All experiments were conducted at a constant p' of 100 kPa and b value of 0.5. To prevent significant stress and strain nonuniformities in the hollow cylinder specimen during shearing, previous studies (Cai 2010; Cai et al. 2018; Hight et al. 1983; Symes 1983) have suggested that the ratio of outer to inner cell pressures should fall within the range of $0.9 \leq p_o/p_i \leq 1.2$. This implies that certain combinations of stresses p', q, and the parameters b and α_σ could not be achieved in the hollow cylinder apparatus. Consequently, based on the stress expressions derived by Hight et al. (1983) and considering the specified range for p_o/p_i, it can be inferred that tests encompassing a variety of α_σ values could be conducted in the HCA when b is set to 0.5, a value commonly adopted in previous studies (Cai et al. 2018; Qian et al. 2018). Throughout the shearing process, the parameters p', b, and α_σ remained constant, with q being incrementally raised at a rate of 1.5 kPa/min, following the protocols outlined in the studies by Cai et al. (2018). A serviceability failure criterion of ε_1-$\varepsilon_3 = 10\%$ was utilized for the strength evaluations. The detailed test program for monotonic tests was outlined in Table 3.

To further investigate the deformation and noncoaxiality, cyclic principal stress rotation (CPSR) tests were performed on sand–rubber mixtures. To ensure that the stress path forms a circle in the $(\sigma_z$-$\sigma_\theta)$-$2\tau_{z\theta}$ plane, as illustrated in Fig. 4(d), $\sqrt{(\sigma_z - \sigma_\theta)^2 + (2\tau_{z\theta})^2} = \sqrt{(\sigma_1 - \sigma_3)^2}$ should be maintained at a constant value throughout the experiment. In this study, σ_1–σ_3 was kept constant at values of 30, 60, and 80 kPa to investigate the effect of stress levels. All specimens were isotropically consolidated at p' value of 100 kPa. Subsequently, the stress difference σ_1–σ_3 was incrementally increased to the target values, and the specimens underwent anisotropic consolidation. The loading step involving CPSR (B-C-D-E-B), as depicted in Fig. 4(d), was carried out under drained conditions. During the CPSR tests, p', b. p' is the mean effective stress and b is the intermediate principal stress coefficient, and σ_1–σ_3, were maintained constant while only α_σ was continuously rotated from 0° to 180° with a rate of 2°/min. This rotation rate is commonly used in previous studies to ensure adequate drainage (Al-rkaby et al. 2017; Yu et al. 2016). Each specimen underwent 10 circular loading cycles. The detailed test program for CPSR tests was summarized in Table 4.

Monotonic Behavior under Inclined Major Principal Stress Axis

Strength Envelope

Fig. 5 summarizes the variation of peak stress ratio (q/p') of sand–rubber mixtures with respect to α_σ values. The detailed stress–strain curves of sand–rubber mixtures at various α_σ values are illustrated in Fig. 6. At $\alpha_\sigma = 2°$, the strength of the sand–rubber mixture decreases as R_c increases. Existing studies have also demonstrated that an increase in the proportion of soft rubber particles results in a decrease in the peak strength of sand–rubber mixtures during triaxial compression testing (Cheng et al. 2023; Ding et al. 2021). When R_c is below the transition rubber content (i.e., approximately 20%), the

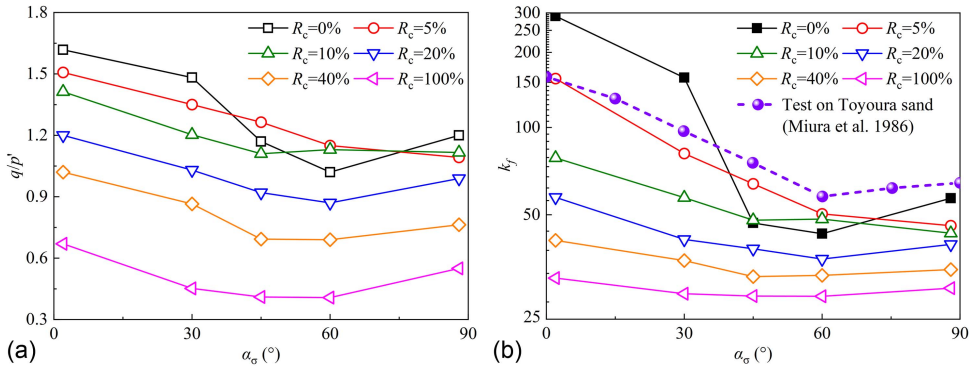

Fig. 5. Variation of peak stress ratio and k_f of sand–rubber mixtures with respect to α_σ values: (a) q/p'; and (b) k_f.

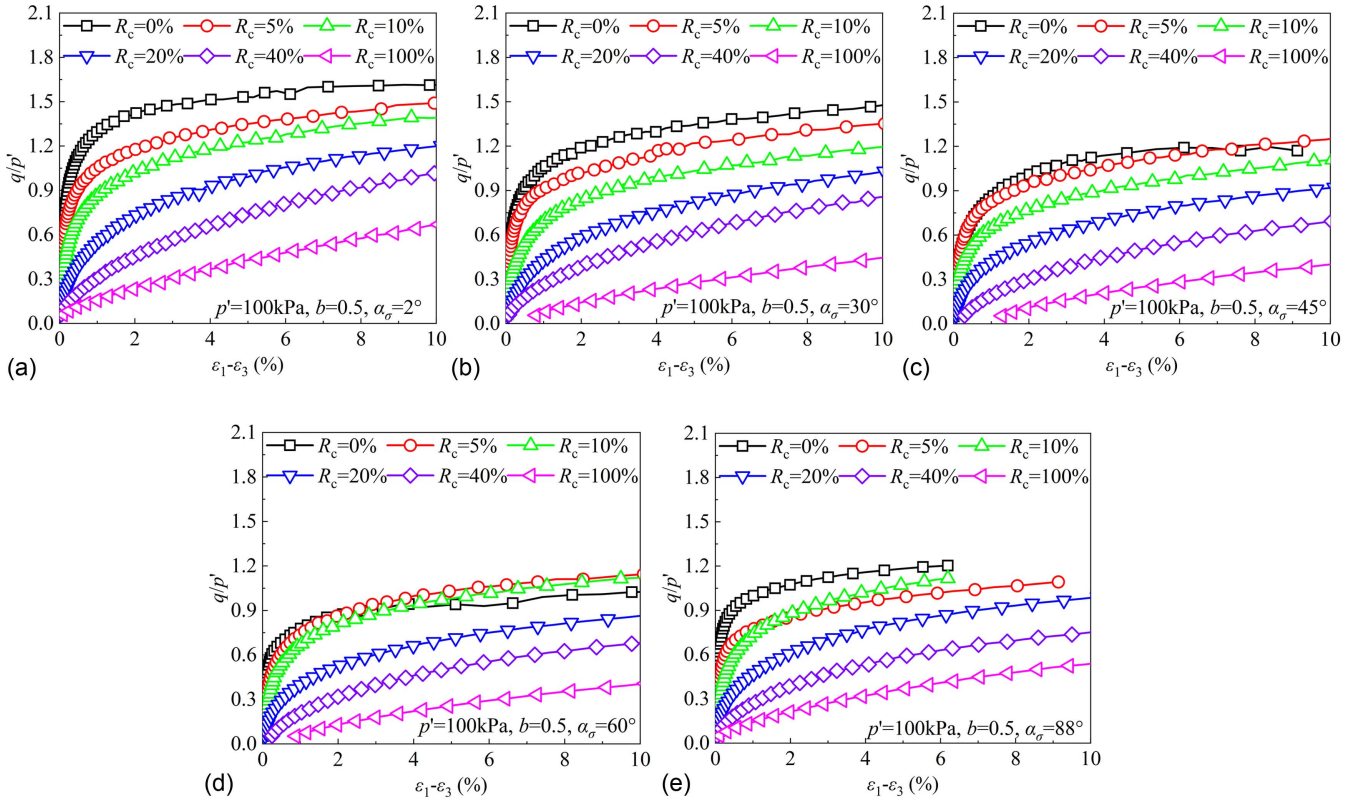

Fig. 6. Stress–strain of mixtures at various α_σ values: (a) $\alpha_\sigma = 2°$; (b) $\alpha_\sigma = 30°$; (c) $\alpha_\sigma = 45°$; (d) $\alpha_\sigma = 60°$; and (e) $\alpha_\sigma = 88°$.

strength of the sand–rubber mixture with well-packed structures experiences a modest decline as R_c decreases. In contrast, when R_c surpasses 20%, there is a marked decrease in the mixture's strength with further increases in R_c. This reduction in strength is due to the dominant role of soft rubber particles in packings once R_c exceeds the transitional rubber content depicted in Fig. 2, which results in loose particle packing, and an increase in sand–rubber and rubber–rubber contacts.

It is clear from Fig. 5 that as α_σ values increase, there is a noticeable decrease in peak strength for clean sand. The lowest strength of clean sand is observed at $\alpha_\sigma = 60°$, consistent with the experimental results reported by Cai et al. (2018) and Xiong et al. (2016), where the lowest peak strength of clean sand falls within the range of approximately $\alpha_\sigma = 60°$–$75°$. Moreover, the compressive strength of clean sand at $\alpha_\sigma = 2°$ is significantly higher than the tensile strength at $\alpha_\sigma = 88°$. Notably, with increasing R_c, the minimum peak strength of sand–rubber mixtures tends to be around $\alpha_\sigma = 45°$. In the $\alpha_\sigma = 30°$–$60°$ range, mixtures with increased R_c exhibit a more gradual change in strength with respect to α_σ. Furthermore, as R_c increases, there is a significant reduction in the difference between the compressive strength at $\alpha_\sigma = 2°$ and the tensile strength at $\alpha_\sigma = 88°$. The above results indicate a notable correlation between the strength dependence on α_σ and the presence of deformable rubber particles.

For further analyze the strength dependence on α_σ values for sand–rubber mixtures, the major, intermediate, and minor principal stresses (i.e., σ_1, σ_2, and σ_3) corresponding to the peak strength of sand–rubber specimens are extracted and depicted in the 3D generalized stress plane, as illustrated in Fig. 7. The Lade–Duncan criterion (Lade and Duncan 1975), detailed in Eq. (4), is applied to describe the strength envelopes (Fig. 7) of sand–rubber mixtures under different loading directions

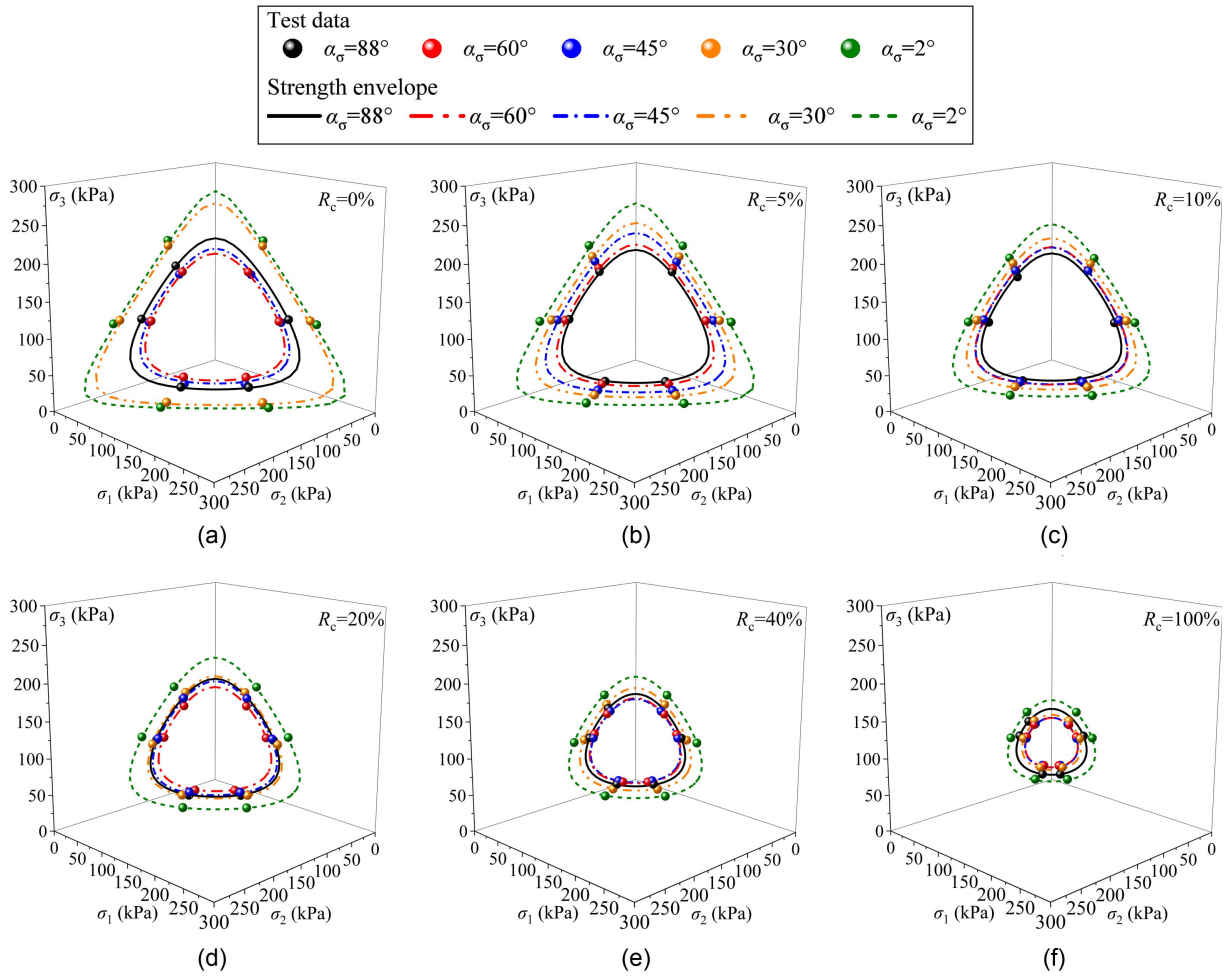

Fig. 7. Strength envelopes of the Lade–Duncan criterion on the π-plane for (a) $R_c = 0\%$; (b) $R_c = 5\%$; (c) $R_c = 10\%$; (d) $R_c = 20\%$; (e) $R_c = 40\%$; and (f) $R_c = 100\%$.

$$\frac{I_1^3}{I_3} = k_f \tag{4}$$

where I_1 and I_3 = first and third invariants of the stress tensor, respectively; and k_f = constant material parameter representing material strength. Calibrating the Lade–Duncan criterion using peak-strength test data of sand–rubber mixtures under varying α_σ values yields different k_f values for the identical material, as presented in Fig. 5(b). Consequently, the failure surface in the π plane also depends on the α_σ value. This dependency is expected, given that material strength is known to vary with α_σ. The variation range of k_f with α_σ reflects the degree of anisotropy of the material (Cao et al. 2017).

The area of strength envelope can be reflected by the k_f values depicted in Fig. 5(b), with larger k_f values corresponding to a larger strength envelope size. As depicted in Figs. 5(b) and 7, it is evident that an increase in R_c not only significantly reduces the area of the failure surface but also alters the degree of anisotropy in the strength envelopes across various loading directions. For the test data of clean sand specimens, including Fujian sand from this study and Toyoura sand from Miura et al. (1986), the range of k_f variation across $\alpha_\sigma = 0°$–$90°$ is considerably broad, signifying a high degree of anisotropy. However, with the increase of R_c, the variation range of k_f within the $\alpha_\sigma = 0°$–$90°$ interval is considerably reduced, suggesting a reduction in anisotropy. This trend is likely a consequence of the rubber particles' inherent isotropic nature. The inherent and induced anisotropy of sand specimens both depend on the anisotropic alignment of particles, which correlates with the preferred orientation of nonspherical particles in the deposition process and concentration of contact normals during plastic deformation, respectively (Oda 1993). Compaction and specimen preparation methods (e.g., deposition, vibration, and tamping) can result in the preferential subhorizontal bedding of sand particles, leading to anisotropic behavior under varying principal stress axis orientations (He et al. 2024). Specifically, the specimen demonstrates its peak strength when the principal stress direction is almost perpendicular to the particle orientation (i.e., at $\alpha_\sigma = 2°$) and its lowest strength when the principal stress direction is nearly parallel to the particle orientation (i.e., at $\alpha_\sigma = 60°$). Oda (1993) indicated that nonspherical sand particles tend to rotate perpendicular to the direction of maximum compression. Besides this rearrangement characteristics of sand particles, the compressibility of rubber particles in all directions enables them to elongate in the direction perpendicular to the maximum compression when subjected to loading. This continuous adjustment of their orientations during loading potentially increases the contact area and promotes the well-packed structures between rubber and sand particles, thereby contributing to interparticle interlocking and friction. Consequently, as the principal stress angle increases within the 0°–90° range,

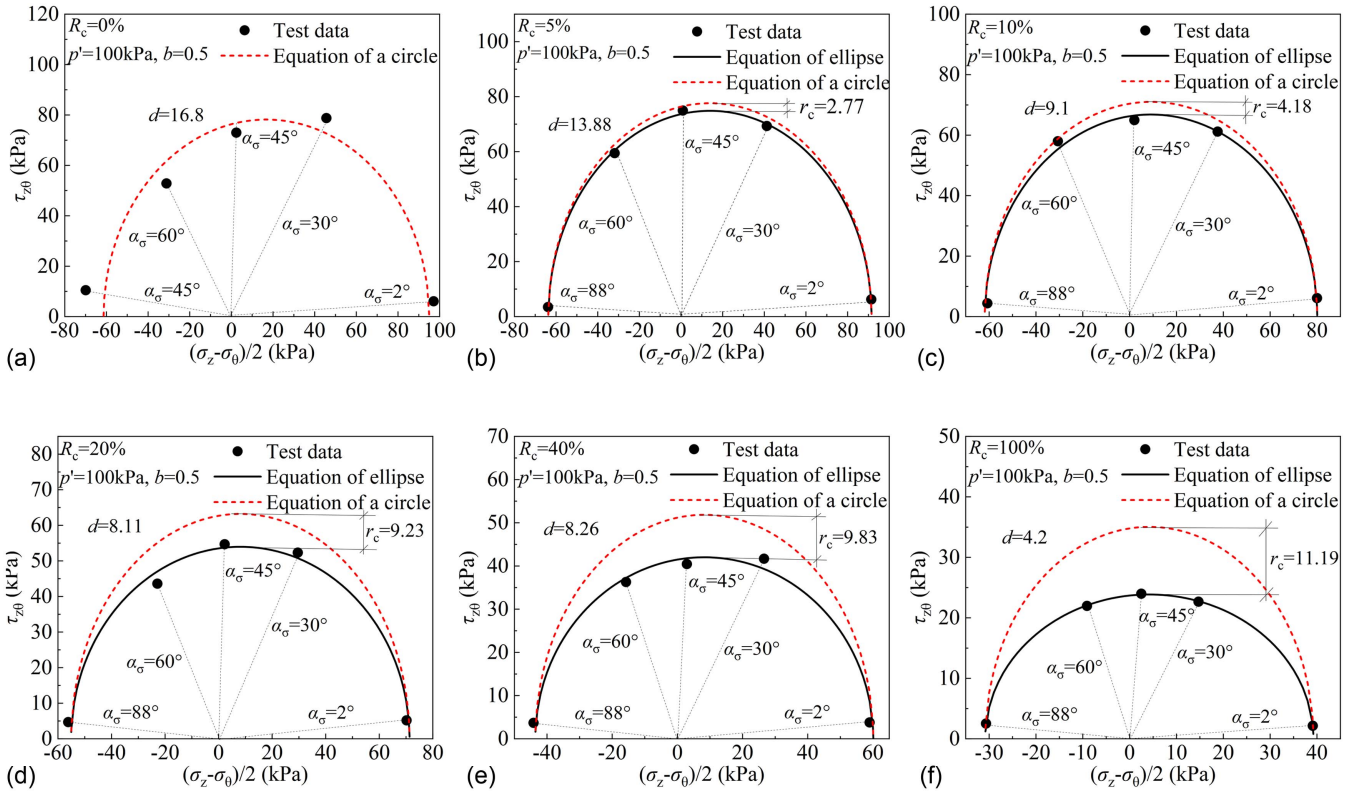

Fig. 8. Strength failure envelopes in $[(\sigma_z\text{-}\sigma_\theta)/2, \tau_{\theta z}]$ stress plane for (a) pure sand; (b) $R_c = 5\%$; (c) $R_c = 10\%$; (d) $R_c = 20\%$; (e) $R_c = 40\%$; and (f) $R_c = 100\%$.

the strength reduction of sand–rubber mixtures compared to clean sand is less significant, leading to reduced anisotropy. This reduced strength degradation and anisotropy due to the inclusion of rubber particles may account for the fact that at α_σ values of 45° and 60°, the strength of the mixture at $R_c = 5\%$–10% is slightly higher than that of clean sand.

Another significant observation from Figs. 7 and 5(b) is that the failure surface area of clean sand exhibits significant changes within the range of $\alpha_\sigma = 30°$–$60°$, with the minimum failure surface area occurring around $\alpha_\sigma = 60°$. Conversely, as R_c increases, the failure surface area shows a much slighter variation and tends to stabilize within the $\alpha_\sigma = 30°$–$60°$ range, with the smallest failure surface area appearing near $\alpha_\sigma = 45°$–$60°$. Moreover, when compared to clean sand, the difference in failure surface sizes of rubber sand under pure tension and compression paths is markedly reduced. Based on the aforementioned analysis, in practical engineering design involving sand–rubber mixtures, the consideration of the strength anisotropy of mixture in safety design can be proportionately reduced as the R_c value increases when using triaxial compressive strength to assess the stability of structures.

The failure points of clean sand, corresponding to the peak stress ratio (q/p') obtained in each test, are also plotted in the $(\sigma_z\text{-}\sigma_\theta)/2$–$\tau_{z\theta}$ plane in Fig. 8(a). The effect of the loading direction on the strength envelope of the sand is demonstrated in this figure. The failure points are not equidistant from the origin of the $(\sigma_z\text{-}\sigma_\theta)/2$–$\tau_{z\theta}$ plane. Furthermore, due to the alignment of particles in the specimen tending to be parallel to the bedding plane and exhibiting initial anisotropy, the specimen's strength along the compressive path exceeds that along the tensile path, resulting in the center of the failure surface of the specimen being biased toward the positive direction of the $(\sigma_z\text{-}\sigma_\theta)/2$–axis. Based on the observation of the test results, Gutierrez et al. (1991) proposed the following failure criterion for sand:

$$\frac{((\sigma_z-\sigma_\theta)/2-d)^2}{r_f^2}+\frac{\tau_{z\theta}^2}{r_f^2}=1 \tag{5}$$

The defined failure surface is a circular shape in the $(\sigma_z\text{-}\sigma_\theta)/2$–$\tau_{z\theta}$ stress space, centered at d with a radius r_f. The parameter d is used to quantify the anisotropy of the sand. For granular materials, the relationship is expressed as $r_f = p' \sin\varphi\text{-}d$, where φ represents the angle of internal friction at failure. The failure points of sand–rubber mixtures are plotted in the $(\sigma_z\text{-}\sigma_\theta)/2$–$\tau_{z\theta}$ plane in Figs. 8(b–f). It can be observed that an increase in R_c results in a notable reduction in $\tau_{z\theta}$ as α_σ approaches 45°. With increasing R_c, the failure surface of the sand–rubber mixture transitions from a circular shape to an ellipse shape with a significantly reduced radius in the $\tau_{z\theta}$-axis direction. Furthermore, the increase in R_c reduces the difference between compressive-direction and tensile-direction strength, causing a decrease in the deviation of the center of the failure surface toward the positive $(\sigma_z\text{-}\sigma_\theta)/2$ axis. Given the aforementioned reasons, the equation for the circle in Eq. (5) is no longer adequate for describing the failure surface of the sand–rubber mixture. Therefore, this study proposes a failure criterion applicable to sand–rubber mixtures utilizing the equation for an ellipse, as outlined below:

$$\frac{((\sigma_z-\sigma_\theta)/2-d)^2}{r_f^2}+\frac{\tau_{z\theta}^2}{(r_f-r_c)^2}=1 \tag{6}$$

The parameter r_c serves as a measure of the decrease in strength components in the torsional direction resulting from the presence of

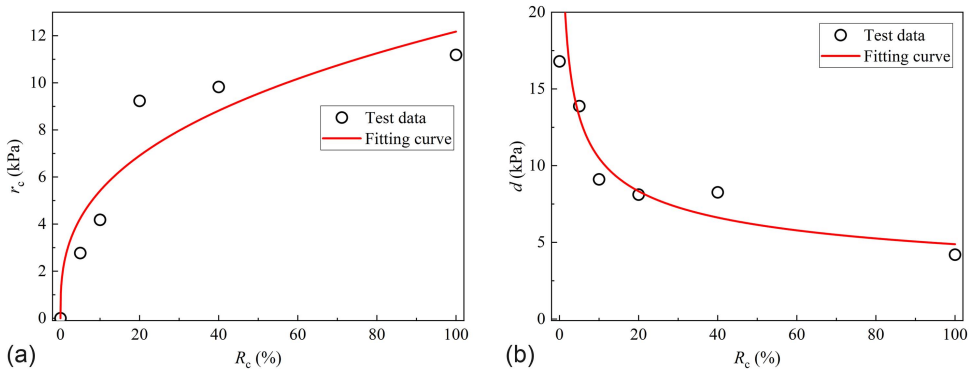

Fig. 9. Correlations between parameters r_c and d with R_c: (a) r_c; and (b) d.

rubber. Figs. 8(b–f) present a comparison between the failure surfaces obtained from Eqs. (5)–(6) and the measured failure points in the $(\sigma_z\text{-}\sigma_\theta)/2\text{–}\tau_{z\theta}$ plane. The findings suggest that Eq. (6) provides a more accurate and appropriate representation of the test data for sand–rubber mixtures when compared to Eq. (5), particularly at high values of R_c. Fig. 9 further illustrates the correlation between parameters r_c and d with R_c. As R_c increases, parameter r_c increases while d decreases, indicating a decrease in the radius of the $\tau_{z\theta}$-axis direction and a weakening of the overall anisotropy of the failure surface.

Deformation Behavior

In addition to affecting monotonic strength, the inclusion of rubber particles is observed to have a significant impact on deformation behavior during monotonic shearing. Note that in this study, positive strain values indicate compression, while negative values indicate tension. Fig. 10 illustrates the relationship between volumetric strain (ε_v) and deviatoric strain (ε_q) of sand–rubber mixtures across various values of α_σ. Clean sand experiences initial contraction followed by dilation across different α_σ values. However, with the increase in R_c, the volumetric strain behavior of the sand–rubber mixture gradually transitions to pure compression behavior, with compressive volumetric strain increasing due to rubber particles' compressibility.

As R_c exceeds the transitional rubber content, the compressive volumetric strain in rubber-dominant specimens with high R_c values of 40% and 100% is lower than that observed in the specimen with $R_c = 20\%$. This difference can be attributed to the lower stress ratio experienced by rubber-dominant specimens, as well as their greater drainage during the consolidation process, which results in a slightly denser state compared to clean sand. It is widely

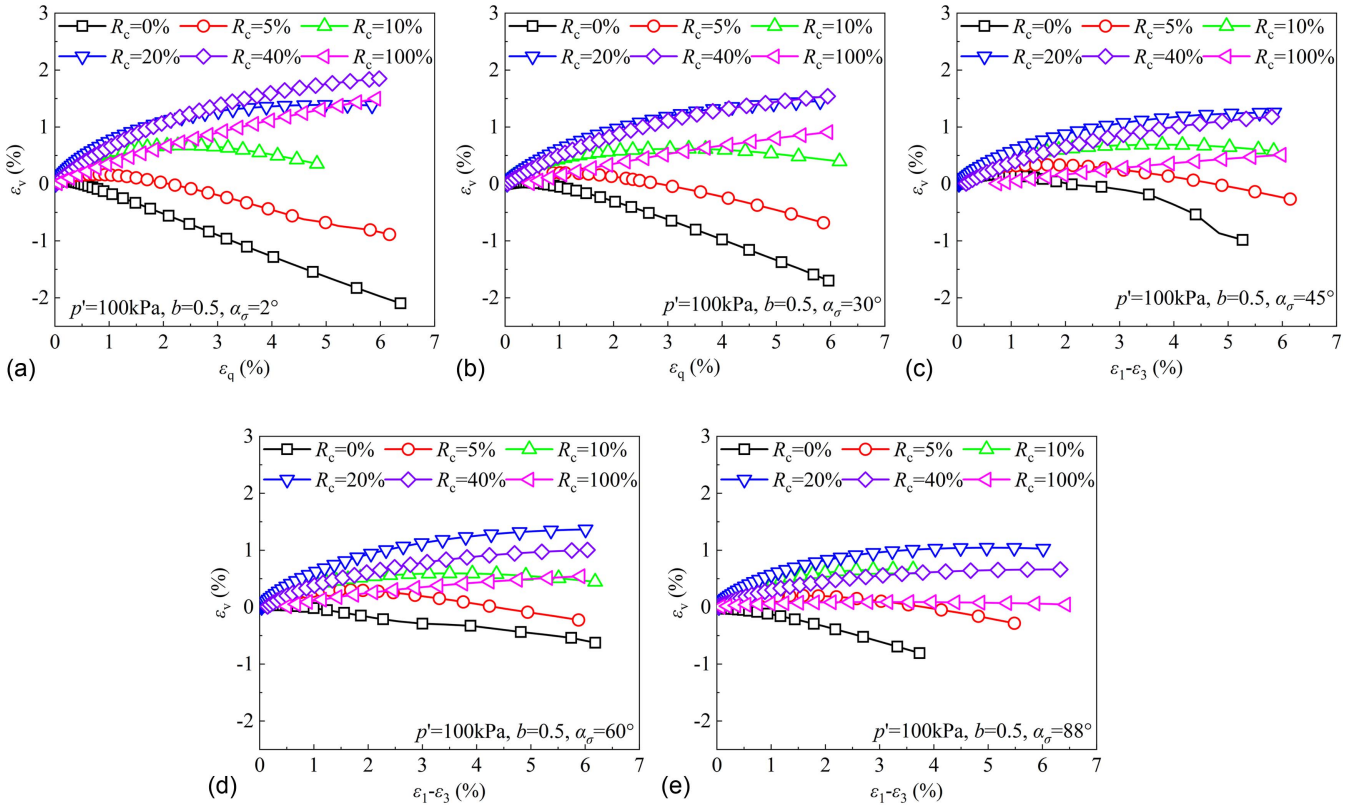

Fig. 10. ε_v versus $\varepsilon_1 - \varepsilon_3$ at different α_σ values: (a) $\alpha_\sigma = 2°$; (b) $\alpha_\sigma = 30°$; (c) $\alpha_\sigma = 45°$; (d) $\alpha_\sigma = 60°$; and (e) $\alpha_\sigma = 88°$.

J. Geotech. Geoenviron. Eng., 2025, 151(11): 04025122

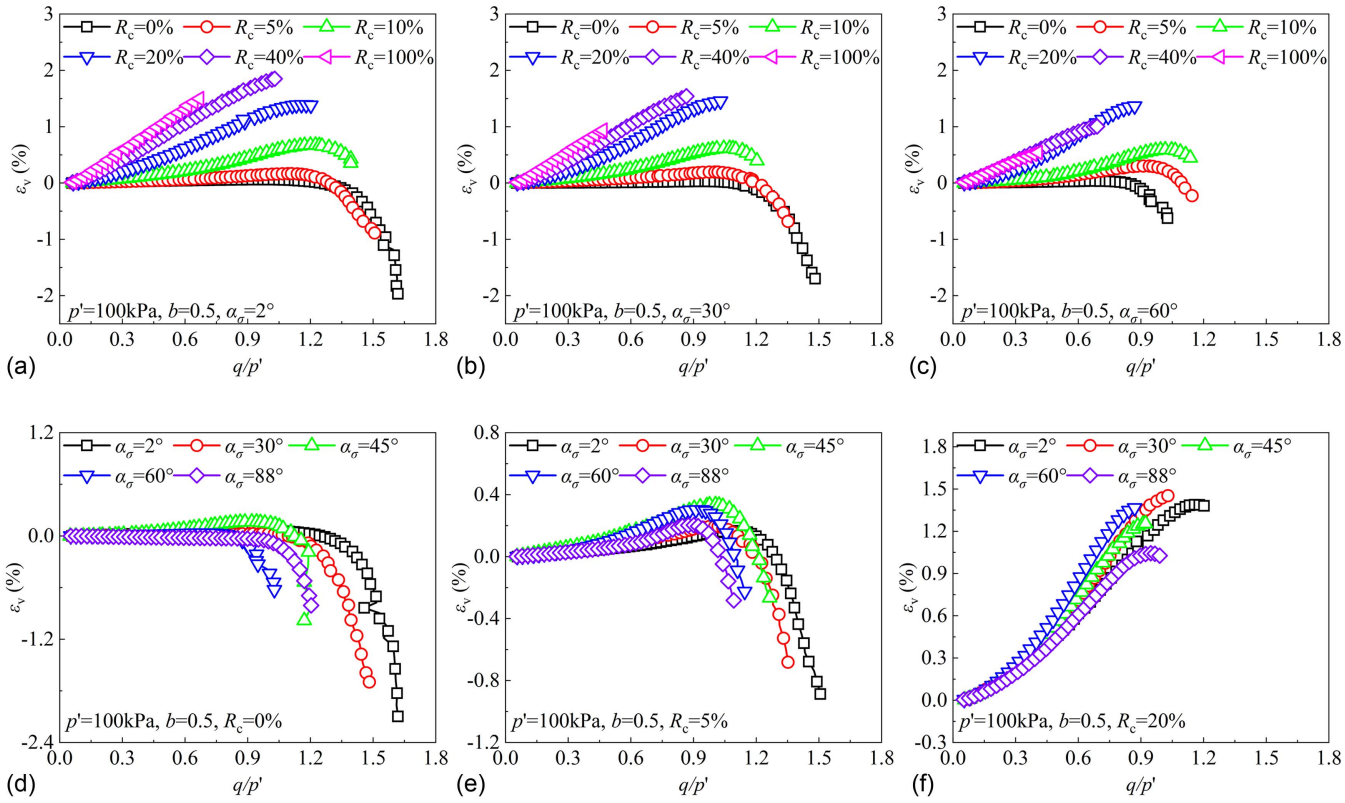

Fig. 11. ε_v versus q/p' under (a) $\alpha_\sigma = 2°$; (b) $\alpha_\sigma = 30°$; (c) $\alpha_\sigma = 60°$; (d) $R_c = 0\%$; (e) $R_c = 5\%$; and (f) $R_c = 20\%$.

acknowledged that the dilatancy of granular materials depends on the stress ratio (Shaverdi et al. 2014). Figs. 11(a–c) present the typical relationships between the stress ratio and volumetric strain of different sand–rubber mixtures under $\alpha_\sigma = 2°$, 30°, and 60°. Under the same stress ratio, an increase in R_c leads to a significant increase in compressive volumetric strain, indicating a more contractive behavior. Figs. 11(d–f) illustrate the relationship between stress ratio and volumetric strain for representative sand–rubber mixtures at different principal stress angles. The dilatancy of sand–rubber mixtures is observed to be influenced by the orientation of the principal stress directions. As α_σ increases, the stress ratio corresponding to the phase transition state of the specimen decreases. Furthermore, with the increase of α_σ, the compressive volumetric strain of the specimen first increases and then slightly decreases when α_σ exceeds approximately 45°–60°.

Cyclic Responses under Pure Principal Stress Rotation

Fig. 12 depicts the changes in various strain components observed during CPSR as a function of the number of loading cycles (N) under different intermediate principal stress coefficients (b). These components include vertical strain (ε_z), torsional shear strain ($\gamma_{z\theta}$), radial strain (ε_r), and circumferential strain (ε_θ). As b increases from 0 to 1, the direction of ε_z development transitions from compression toward tension, while the direction of ε_r development transitions from tension direction toward compression direction owing to the strengthened confinement in the radial direction. Irrespective of b values, the variation of $\gamma_{z\theta}$ with respect to N exhibits fluctuations about the 0 axis [Figs. 12(d–f)], without significant plastic accumulation. Moreover, from Fig. 16, it is evident that as R_c increases, all strain components increase, indicating the adverse impact of incorporating compressible rubber particles on deformation behavior under pure principal stress rotation.

Figs. 13(a and b), Figs. 13(c and d), Figs. 13(e and f), and Figs. 13(g and h) respectively compare the vertical strain, torsional shear strain, radial strain, and circumferential strain with respect to the variation of N for σ_1–$\sigma_3 = 30$ kPa and σ_1–$\sigma_3 = 80$ kPa. The results for σ_1–$\sigma_3 = 60$ kPa can be found in Fig. 12. With increasing stress levels, all strain components of the sand–rubber mixture increase. Fig. 14 illustrates the volumetric strain of the sand–rubber mixture under CPSR as a function of N. It can be observed that with the increase in R_c, the volumetric strain of the sand–rubber mixture monotonically increases, irrespective of stress levels and b values.

Noncoaxiality Characteristics

The importance of considering the noncoaxiality between the axes of principal stress and principal strain increment in modeling soil behavior has been highlighted by Cai (2010). Accurately predicting both the magnitude and direction of soil deformation during the design stages of geotechnical engineering is important, as overlooking noncoaxiality may result in unreliable designs. Investigating the mechanical response of soils under CPSR is widely regarded as a valuable approach for understanding soil noncoaxiality. Fig. 15 illustrates the typical variation of the noncoaxiality angle (β) with α_σ under CPSR, utilizing three sand–rubber mixtures as examples. It is evident that as α_σ increases from 0° to 180°, a significant noncoaxiality angle arises and fluctuates due to material anisotropy. With an increase in parameter N, the β value of the sand–rubber mixture experiences a slight increase. Fig. 16 depicts the influence of stress level σ_1–σ_3 on the noncoaxiality angle under CPSR, employing three sand–rubber mixtures as illustrative examples. It is apparent that β decreases as σ_1–σ_3 increases. This reduced level of noncoaxiality at

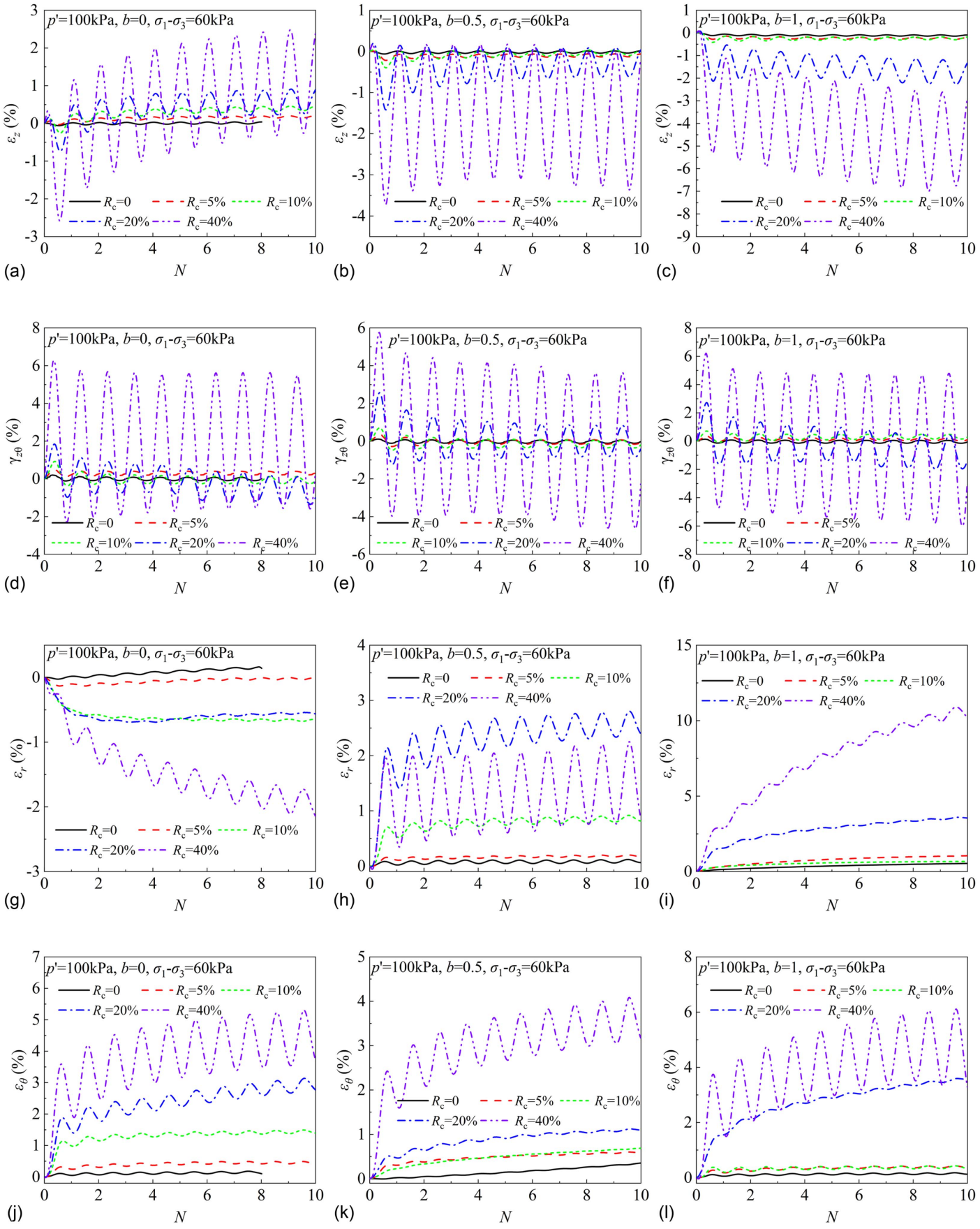

Fig. 12. Various strain components versus N of mixtures ($p' = 100$ kPa, $\sigma_1 - \sigma_3 = 60$ kPa): (a)–(c) ε_z at $b = 0$, 0.5, and 1, respectively; (d)–(f) $\gamma_{z\theta}$ at $b = 0$, 0.5, and 1, respectively; (g) –(i) ε_r at $b = 0$, 0.5, and 1, respectively; and (j)–(l) ε_θ at $b = 0$, 0.5, and 1, respectively.

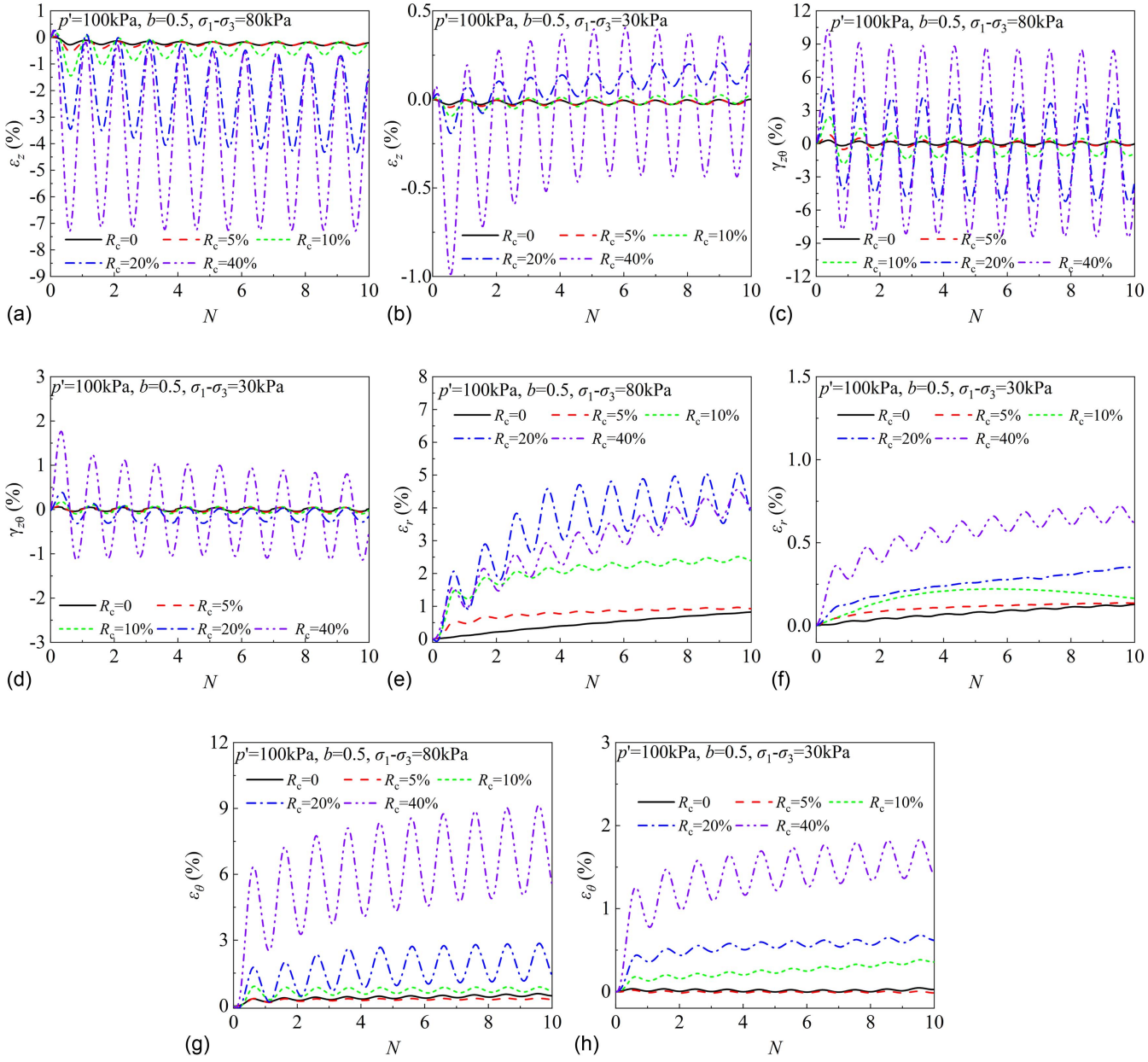

Fig. 13. Various strain components versus N of mixtures ($p' = 100$ kPa, $b = 0.5$): (a and b) ε_z at $\sigma_1 - \sigma_3 = 30$ kPa and $\sigma_1 - \sigma_3 = 80$ kPa, respectively; (c and d) $\gamma_{z\theta}$ at $\sigma_1 - \sigma_3 = 30$ kPa and $\sigma_1 - \sigma_3 = 80$ kPa, respectively; (e and f) ε_r at $\sigma_1 - \sigma_3 = 30$ kPa and $\sigma_1 - \sigma_3 = 80$ kPa, respectively; and (g and h) ε_θ at $\sigma_1 - \sigma_3 = 30$ kPa and $\sigma_1 - \sigma_3 = 80$ kPa, respectively.

higher stress levels can be attributed to the variation in anisotropic structure formation, as elucidated by Li and Yu (2010) from a discrete element method perspective. Additionally, Fig. 17 depicts the influence of intermediate principal stress coefficient (b) on the noncoaxiality angle under CPSR, employing three sand–rubber mixtures as illustrative examples. As observed, b has an insignificant effect on the noncoaxiality of granular materials.

Fig. 18 compares the variation of the noncoaxiality angle with α_σ during CPSR for different sand–rubber mixtures at various stress conditions, employing the case of $N = 2$ as illustrative examples. It can be clearly observed that the inclusion of rubber particles has a significant impact on reducing noncoaxiality. Specifically, as R_c increases, the noncoaxiality angle of the specimen decreases. However, once R_c exceeds a certain threshold, further increase in R_c leads to a slight increase of the noncoaxiality angle. This is likely attributed to the increased contact area and coordination number in sand–rubber contacts due to the presence of deformable rubber particles, leading to a more uniform and isotropic deformation of sand–rubber mixtures during CPSR compared to clean sand. Nevertheless, as R_c exceeds the transitional rubber content value, the rubber–rubber contacts significantly decrease, thereby compromising this interlocking effect.

Several key points extracted from Fig. 18, such as the noncoaxiality angles corresponding to $\alpha_\sigma = 0°$, $\alpha_\sigma = 45°$, $\alpha_\sigma = 90°$, $\alpha_\sigma = 135°$, and $\alpha_\sigma = 180°$, are plotted as functions of R_c and shown in Fig. 19. It is evident that at σ_1–$\sigma_3 = 30$ kPa, the noncoaxiality angles at various key points initially decrease with R_c, and then slightly increase, reaching a minimum at $R_c = 20\%$. As observed from Fig. 19, with an increase in σ_1–σ_3, the increase in noncoaxiality angle with R_c becomes more significant when R_c exceeds the threshold value. Particularly, at σ_1–$\sigma_3 = 80$ kPa, the minimum value of the noncoaxiality angle appears earlier at $R_c = 10\%$, and when R_c

J. Geotech. Geoenviron. Eng., 2025, 151(11): 04025122

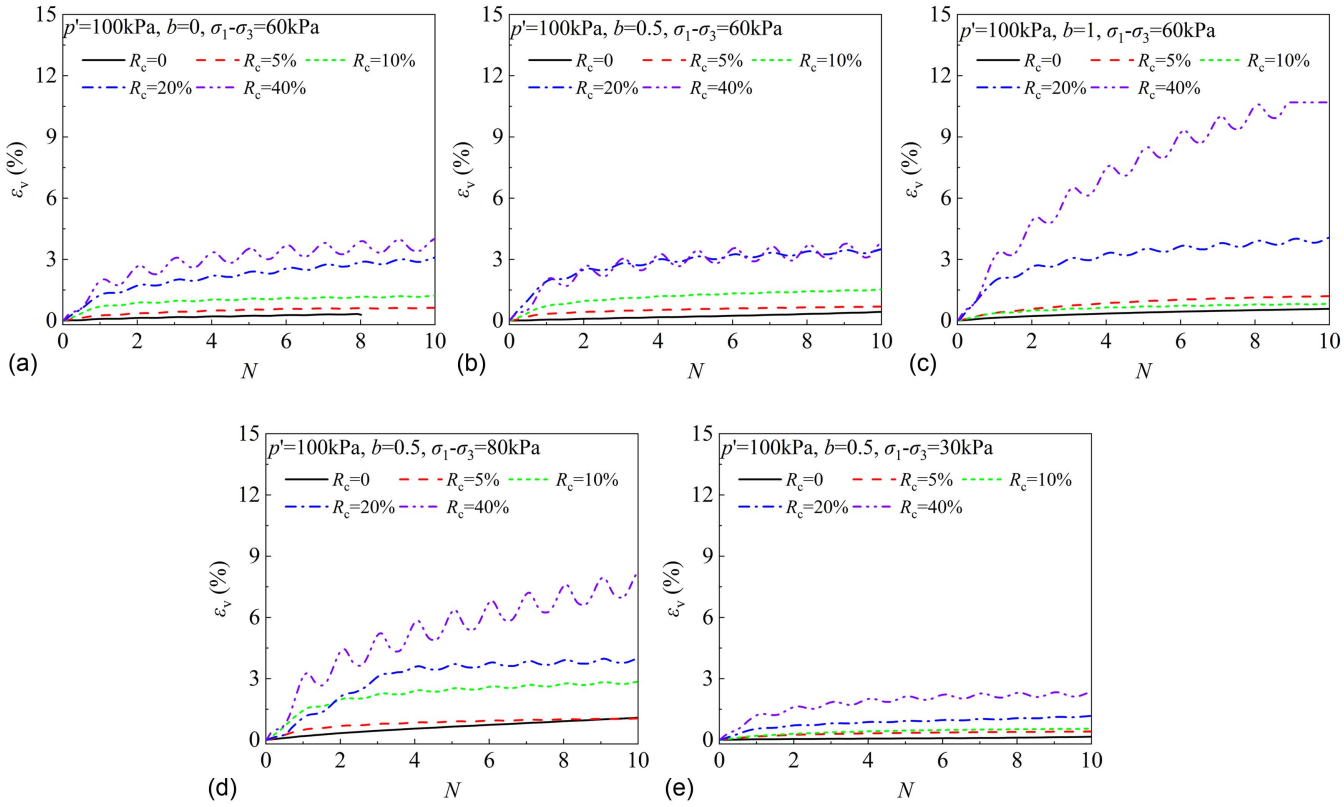

Fig. 14. Volumetric strain (ε_v) versus N of mixtures ($p' = 100$ kPa): (a) $b = 0$, $\sigma_1 - \sigma_3 = 60$ kPa; (b) $b = 0.5$, $\sigma_1 - \sigma_3 = 60$ kPa; (c) $b = 1$, $\sigma_1 - \sigma_3 = 60$ kPa; (d) $b = 0.5$, $\sigma_1 - \sigma_3 = 80$ kPa; and (e) $b = 0.5$, $\sigma_1 - \sigma = 30$ kPa.

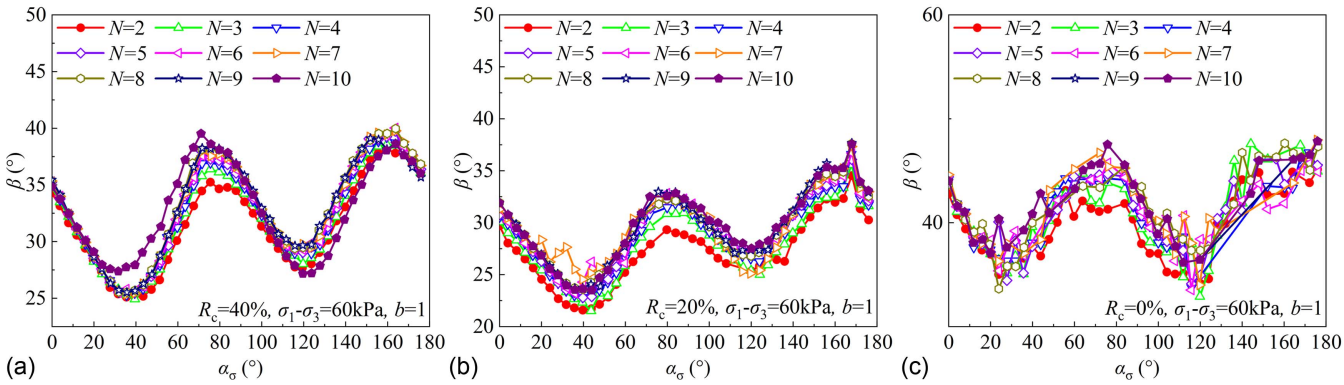

Fig. 15. β versus α_σ of mixtures ($p' = 100$ kPa, $\sigma_1 - \sigma_3 = 60$ kPa, $b = 1$) under different N values for (a) $R_c = 40\%$; (b) $R_c = 20\%$; and (c) $R_c = 0\%$.

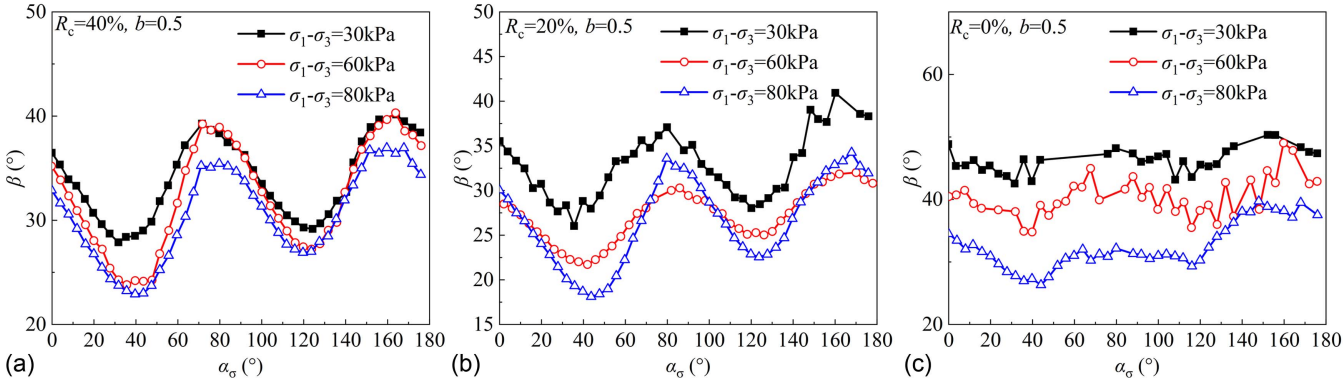

Fig. 16. β versus α_σ of mixtures ($b = 0.5$) under different $\sigma_1 - \sigma_3$ values for (a) $R_c = 40\%$; (b) $R_c = 20\%$; and (c) $R_c = 0\%$.

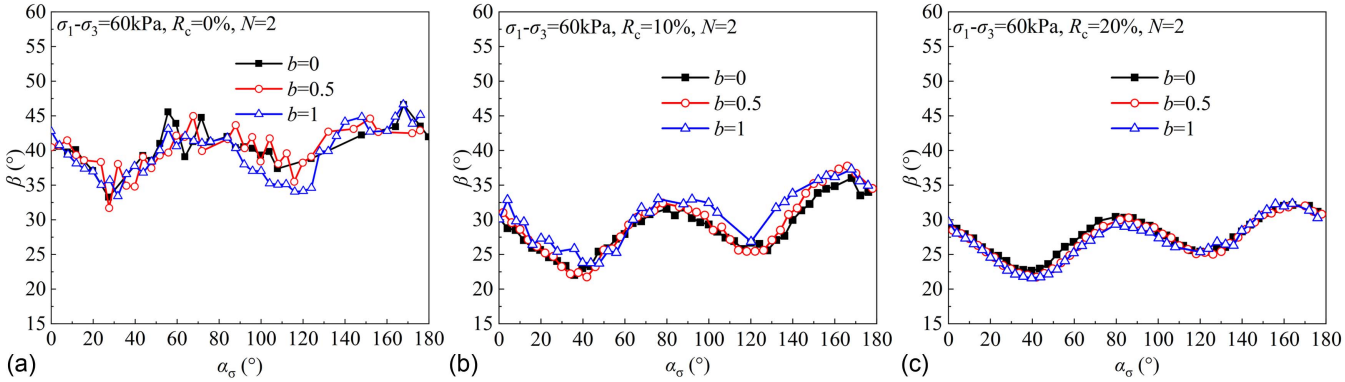

Fig. 17. β versus α_σ of mixtures ($\sigma_1 - \sigma_3 = 60$ kPa) under different b values for (a) $R_c = 0\%$; (b) $R_c = 10\%$; and (c) $R_c = 20\%$.

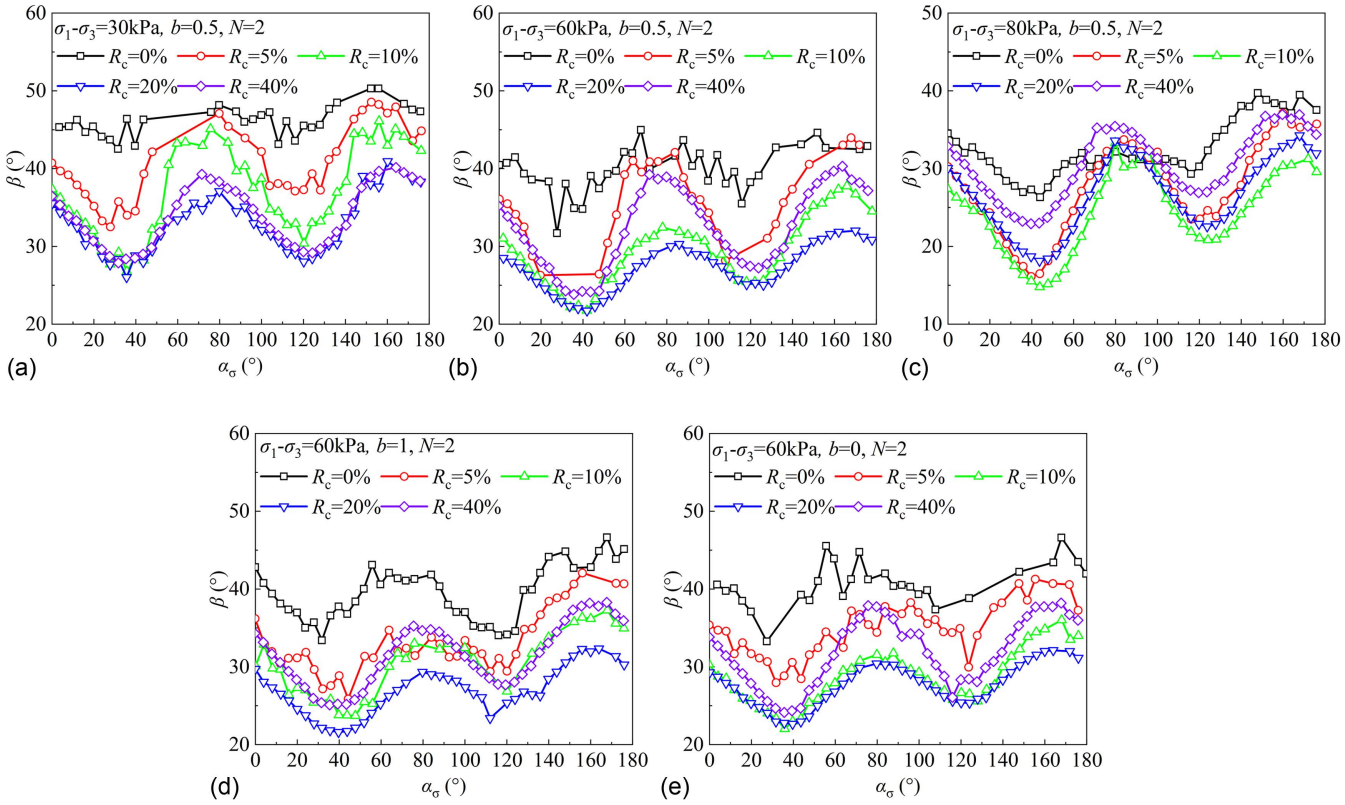

Fig. 18. β versus α_σ of mixtures ($N = 2$) under different R_c values: (a) $b = 0.5$, $\sigma_1 - \sigma_3 = 30$ kPa; (b) $b = 0.5$, $\sigma_1 - \sigma_3 = 60$ kPa; (c) $b = 0.5$, $\sigma_1 - \sigma_3 = 80$ kPa; (d) $b = 1$, $\sigma_1 - \sigma_3 = 60$ kPa; and (e) $b = 0$, $\sigma_1 - \sigma_3 = 60$ kPa.

exceeds 10%, the increase in noncoaxiality angle with R_c becomes more severe compared to the cases of σ_1–$\sigma_3 = 30$ kPa and σ_1–$\sigma_3 = 60$ kPa. This suggests that an increase in stress level reduces the effectiveness of adding rubber particles in reducing noncoaxiality. Moreover, the influence of adding rubber particles on the material's noncoaxiality is independent of b, as observed from Figs. 19(b, d, and e). The remarkable findings in Fig. 19 illustrate the impact of adding rubber particles in reducing noncoaxiality of granular materials under CPSR. Specifically, the addition of rubber particles can cause the maximum reduction in the noncoaxiality angle of nearly 18° compared to clean sand, a change that outweighs the influence of other factors such as stress levels. This aspect should be thoroughly considered in practical engineering applications.

Fig. 20 further illustrates the variation of noncoaxiality angle with stress ratio in monotonic shear. When vertical stress and torsional shear stress are simultaneously applied, for example, at $\alpha_\sigma = 30°$ and $\alpha_\sigma = 60°$ [see Figs. 20(a and b)], the noncoaxiality of the granular material is robust. With an increase in stress ratio, the noncoaxiality angle of the sand–rubber mixture decreases. In Figs. 20(a and b), it can be observed that with an increase in R_c, the noncoaxiality of the material in monotonic shear first decreases and then slightly increases. Figs. 20(c and d) show the variation of noncoaxiality angle of sand–rubber mixture with stress ratio at $\alpha_\sigma = 2°$ and $\alpha_\sigma = 45°$. In Figs. 20(c and d), when only vertical stress or torsional shear stress is applied, although the material's noncoaxiality is relatively low, it can still be seen that the inclusion of rubber particles can reduce the noncoaxiality angle during initial loading stage.

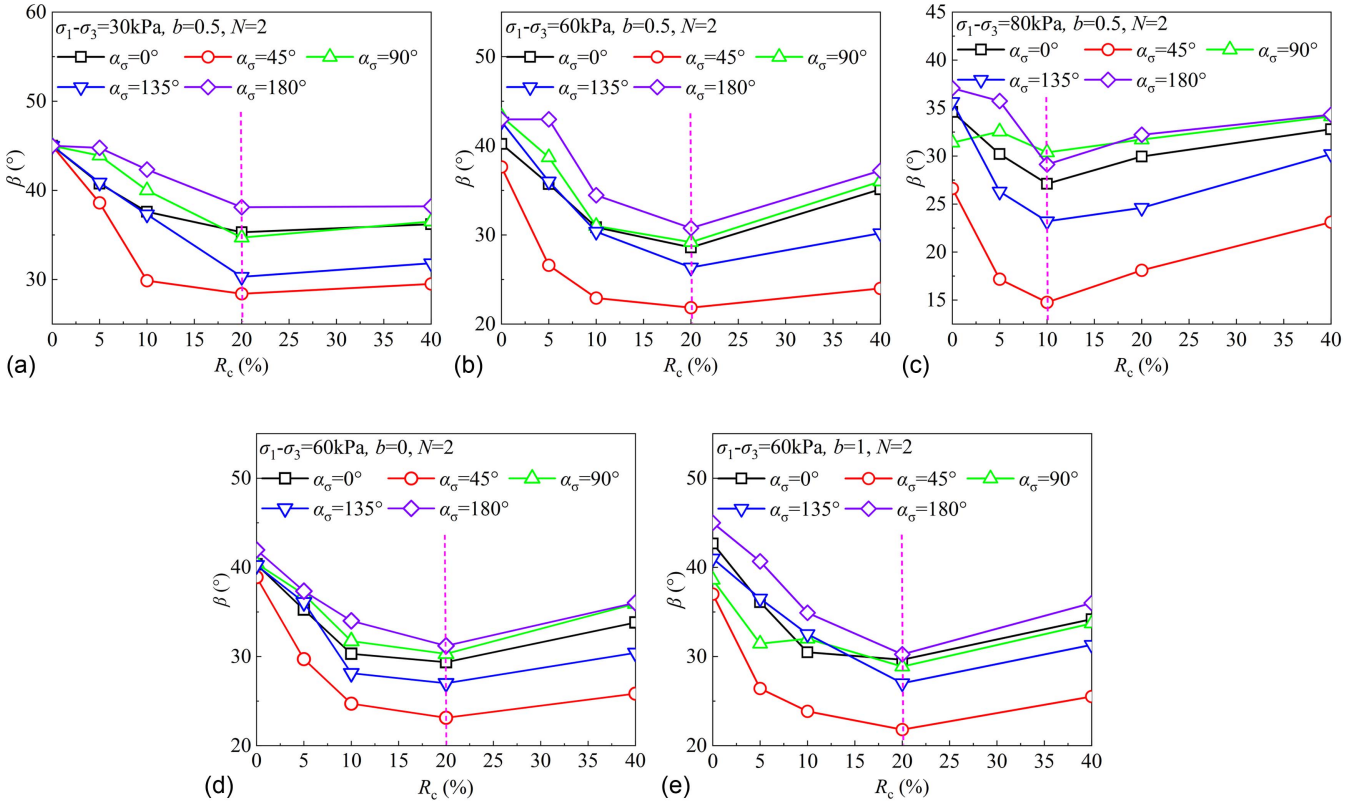

Fig. 19. β of key points versus R_c of mixtures ($N = 2$) under (a) $b = 0.5$, $\sigma_1 - \sigma_3 = 30$ kPa; (b) $b = 0.5$, $\sigma_1 - \sigma_3 = 60$ kPa; (c) $b = 0.5$, $\sigma_1 - \sigma_3 = 80$ kPa; (d) $b = 0$, $\sigma_1 - \sigma_3 = 60$ kPa; and (e) $b = 1$, $\sigma_1 - \sigma_3 = 60$ kPa.

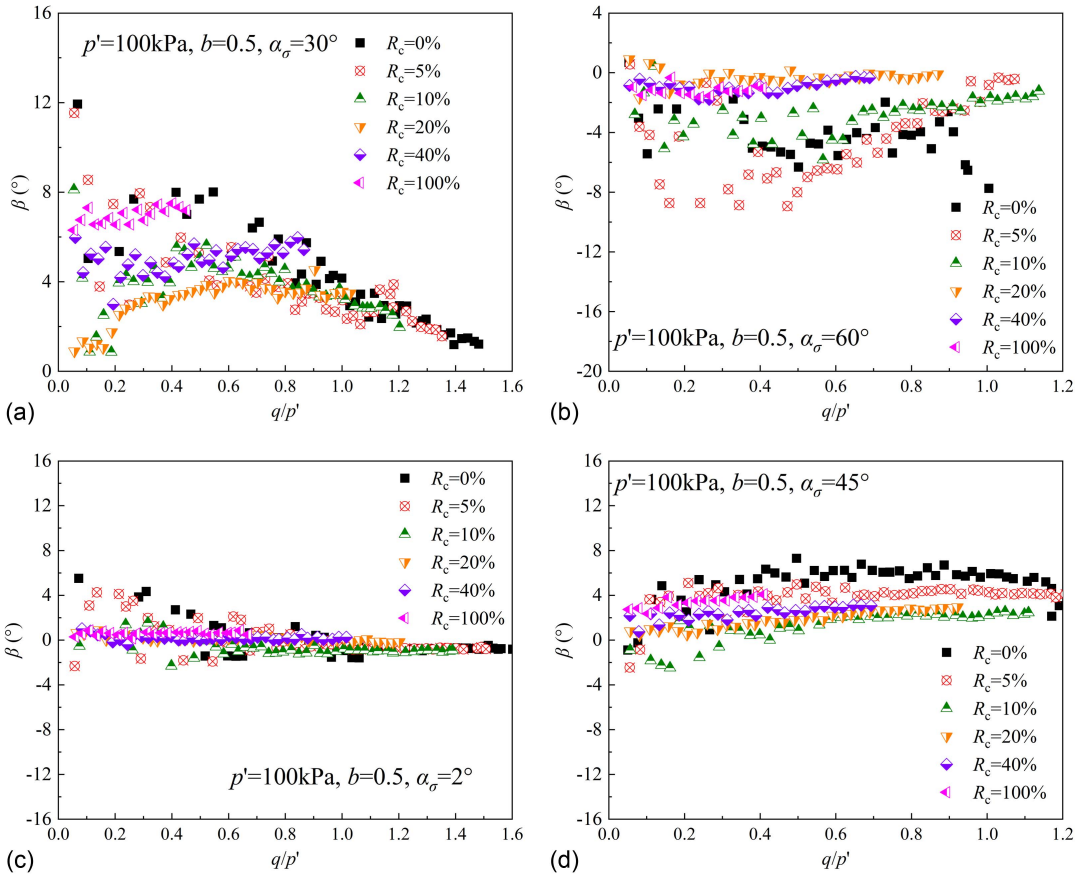

Fig. 20. β versus q/p' of mixtures under monotonic shearing: (a) $\alpha_\sigma = 30°$; (b) $\alpha_\sigma = 60°$; (c) $\alpha_\sigma = 2°$; and (d) $\alpha_\sigma = 45°$.

Conclusions

A hollow cylinder torsional shear experimental program was conducted to examine the strength and deformation characteristics of sand–rubber mixtures with varying rubber contents (R_c). This program comprised monotonic drained tests with different α_σ values, along with cyclic drained tests involving CPSR stress path. The analysis of the experimental data led to the following conclusions:

- The inclusion of granulated rubber significantly impacted the strength anisotropy under different principal stress axis directions (α_σ). As the rubber content (R_c) increased, the anisotropy of strength envelopes within generalized stress plane with respect to α_σ values notably reduced, attributable to the isotropic characteristics of the rubber particles. The minimum strength of clean sand typically occurred around $\alpha_\sigma = 60°$, whereas for sand–rubber mixtures, it tended to happen around $\alpha_\sigma = 45°$. The failure surface of clean sand in the $(\sigma_z\text{-}\sigma_\theta)/2\text{–}\tau_{z\theta}$ plane could be represented by an equation of an asymmetric circle. As R_c increased, the failure surface of the mixture transitioned from a circular to an elliptical shape with a notably reduced radius in the $\tau_{z\theta}$-axis direction. Moreover, the rise in R_c reduced the anisotropy between compressive strength and tensile strength, leading to a decrease in the deviation of the failure surface center in the $(\sigma_z\text{-}\sigma_\theta)/2$ axis. Consequently, an equation suitable for characterizing the failure surface of rubber mixtures was proposed.
- Clean sand exhibited initial contraction followed by dilation across various α_σ values. However, as R_c increased, the volumetric strain behavior of the sand–rubber mixtures shifted gradually toward pure compression. Under identical stress ratios, an increase in R_c resulted in a marked increase in compressive volumetric strain. The dilatancy of sand–rubber mixtures was influenced by the orientation of the principal stress directions. With an increase in α_σ, the stress ratio at the phase transition state of the specimen decreased.
- Under a CPSR stress path, an increase in R_c would lead to higher strain components. In the context of CPSR, the addition of rubber particles had a significant effect in reducing the mixture's noncoaxiality. With the increase in R_c, the noncoaxiality of the mixture initially decreased and then slightly increased. The increase in stress levels would weaken the reduction effect of rubber particles on noncoaxiality. This reduction effect of rubber particles on noncoaxiality was also observed in monotonic shear tests

Data Availability Statement

Some or all data, models, or code that support the findings of this study are available from the corresponding author upon reasonable request.

Acknowledgments

This research was financially supported by the Research Grants Council (RGC) of Hong Kong Special Administrative Region Government (HKSARG) of China (grant Nos. 15220221, 15226822, and 15227923).

References

Ahmad, A., and K. Fakharian. 2020. "Effect of stress rotation and intermediate stress ratio on monotonic behavior of granulated rubber–sand mixtures." *J. Mater. Civ. Eng.* 32 (4): 04020047. https://doi.org/10.1061/(ASCE)MT.1943-5533.0003054.

Al-rkaby, A. H. J., A. Chegenizadeh, and H. R. Nikraz. 2017. "Cyclic behavior of reinforced sand under principal stress rotation." *J. Rock Mech. Geotech. Eng.* 9 (4): 585–598. https://doi.org/10.1016/j.jrmge.2017.03.010.

Ari, A., and S. Akbulut. 2022. "Effect of particle size and shape on shear strength of sand–rubber granule mixtures." *Granular Matter* 24 (4): 126. https://doi.org/10.1007/s10035-022-01287-7.

Ari, A., and S. Akbulut. 2024. "Investigation of micro-scale shear response of sand–rubber granule mixture in terms of particle shape and grain scale deformability effects." *Particuology* 90 (Jul): 452–469. https://doi.org/10.1016/j.partic.2024.01.013.

Asadi, M., A. Mahboubi, and K. Thoeni. 2018. "Discrete modeling of sand–tire mixture considering grain-scale deformability." *Granular Matter* 20 (2): 18. https://doi.org/10.1007/s10035-018-0791-4.

Cai, Y. 2010. "An experimental study of non-coaxial soil behaviour using hollow cylinder testing." Ph.D. dissertation, Dept. of Civil Engineering, Univ. of Nottingham.

Cai, Y., X. Song, Q. Sun, Q. Dong, and J. Wang. 2018. "Drained responses of granular soil sheared under inclined principal stress axes: Impact of sample preparation." *Eng. Geol.* 241 (Jul): 33–40. https://doi.org/10.1016/j.enggeo.2018.05.002.

Cai, Y., H.-S. Yu, D. Wanatowski, and X. Li. 2013. "Noncoaxial behavior of sand under various stress paths." *J. Geotech. Geoenviron. Eng.* 139 (8): 1381–1395. https://doi.org/10.1061/(ASCE)GT.1943-5606.0000854.

Cao, W., R. Wang, and J.-M. Zhang. 2017. "Formulation of anisotropic strength criteria for cohesionless granular materials." *Int. J. Geomech.* 17 (7): 04016151. https://doi.org/10.1061/(ASCE)GM.1943-5622.0000861.

Cheng, Z., J. Wang, B. Zhou, and W. Xiong. 2023. "The micro-mechanical behaviour of sand–rubber mixtures under shear: A numerical study based on X-ray micro-tomography." *Comput. Geotech.* 163 (Nov): 105714. https://doi.org/10.1016/j.compgeo.2023.105714.

Chinese Standard. 2019. *Standard for geotechnical testing method*. GB/T 50123-2019. Beijing: Chinese Standard Press.

Dai, B., Y. Chen, D. Chang, J. Yang, and J. Liu. 2024. "Experimental study on the critical-state and energy dissipation behaviors of rubber-sand mixtures." *Int. J. Geomech.* 24 (3): 04023294. https://doi.org/10.1061/IJGNAI.GMENG-8818.

Dai, B.-B., Q. Liu, X. Mao, P.-Y. Li, and Z.-Z. Liang. 2023. "A reinterpretation of the mechanical behavior of rubber-sand mixtures in direct shear testing." *Constr. Build. Mater.* 363 (Jan): 129771. https://doi.org/10.1016/j.conbuildmat.2022.129771.

Ding, Y., J. Zhang, X. Chen, X. Wang, and Y. Jia. 2021. "Experimental investigation on static and dynamic characteristics of granulated rubber-sand mixtures as a new railway subgrade filler." *Constr. Build. Mater.* 273 (Mar): 121955. https://doi.org/10.1016/j.conbuildmat.2020.121955.

Feng, D., and J. Zhang. 2023. "Non-coaxiality behaviours and unified flow rule of soil-structure interfaces." *Géotechnique* 75 (1): 85–93. https://doi.org/10.1680/jgeot.22.00413.

Fu, R., M. R. Coop, and X. Q. Li. 2014. "The mechanics of a compressive sand mixed with tyre rubber." *Géotech. Lett.* 4 (3): 238–243. https://doi.org/10.1680/geolett.14.00027.

Fu, R., M. R. Coop, and X. Q. Li. 2017. "Influence of particle type on the mechanics of sand-rubber mixtures." *J. Geotech. Geoenviron. Eng.* 143 (9): 04017059. https://doi.org/10.1061/(ASCE)GT.1943-5606.0001680.

Gao, Z., and J. Zhao. 2012. "Efficient approach to characterize strength anisotropy in soils." *J. Eng. Mech.* 138 (12): 1447–1456. https://doi.org/10.1061/(ASCE)EM.1943-7889.0000451.

Gutierrez, M., K. Ishihara, and I. Towhata. 1991. "Flow theory for sand during rotation of principal stress direction." *Soils Found.* 31 (4): 121–132. https://doi.org/10.3208/sandf1972.31.4_121.

He, S.-H., Z.-Y. Yin, Z. Ding, and R.-D. Li. 2024. "Particle morphology and principal stress direction dependent strength anisotropy through torsional shear testing." *Can. Geotech. J.* 62 (Jan): 1–23. https://doi.org/10.1139/cgj-2023-0717.

He, S.-H., Z.-Y. Yin, E. Ibraim, and Z. Ding. 2025. "Face mask chips-reinforced sands under monotonic and cyclic torsional shearing." *Géotechnique* (Mar): 1–46. https://doi.org/10.1680/jgeot.24.01180.

Hight, D. W., A. Gens, and M. J. Symes. 1983. "The development of a new hollow cylinder apparatus for investigating the effects of principal stress rotation in soils." *Géotechnique* 33 (4): 355–383. https://doi.org/10.1680/geot.1983.33.4.355.

Huang, M., X. Lu, and J. Qian. 2010. "Non-coaxial elasto-plasticity model and bifurcation prediction of shear banding in sands." *Int. J. Numer. Anal. Methods Geomech.* 34 (9): 906–919. https://doi.org/10.1002/nag.838.

Japanese Geotechnical Society Standards. 2020. *Practice for preparing hollow cylindrical specimens of soils for torsional shear test*. JGS-0550-2020. Tokyo: Japanese Geotechnical Society.

Kim, H.-K., and J. C. Santamarina. 2008. "Sand–rubber mixtures (large rubber chips)." *Can. Geotech. J.* 45 (10): 1457–1466. https://doi.org/10.1139/T08-070.

Lade, P. V., and J. M. Duncan. 1975. "Elastoplastic stress-strain theory for cohesionless soil." *J. Geotech. Eng. Div.* 101 (10): 1037–1053. https://doi.org/10.1061/AJGEB6.0000204.

Lee, C., H. Shin, and J.-S. Lee. 2014. "Behavior of sand–rubber particle mixtures: Experimental observations and numerical simulations." *Int. J. Numer. Anal. Methods Geomech.* 38 (16): 1651–1663. https://doi.org/10.1002/nag.2264.

Li, W., C. Y. Kwok, C. S. Sandeep, and K. Senetakis. 2019. "Sand type effect on the behaviour of sand-granulated rubber mixtures: Integrated study from micro- to macro-scales." *Powder Technol.* 342 (Jan): 907–916. https://doi.org/10.1016/j.powtec.2018.10.025.

Li, X., and H.-S. Yu. 2010. "Numerical investigation of granular material behaviour under rotational shear." *Géotechnique* 60 (5): 381–394. https://doi.org/10.1680/geot.2010.60.5.381.

Mashiri, M. S., J. S. Vinod, M. N. Sheikh, and H.-H. Tsang. 2015. "Shear strength and dilatancy behaviour of sand–tyre chip mixtures." *Soils Found.* 55 (3): 517–528. https://doi.org/10.1016/j.sandf.2015.04.004.

Miura, K., S. Miura, and S. Toki. 1986. "Deformation behavior of anisotropic dense sand under principal stress axes rotation." *Soils Found.* 26 (1): 36–52. https://doi.org/10.3208/sandf1972.26.36.

Oda, M. 1993. "Inherent and induced anisotropy in plasticity theory of granular soils." *Mech. Mater.* 16 (1): 35–45. https://doi.org/10.1016/0167-6636(93)90025-M.

Pamukcu, S., and S. Akbulut. 2006. "Thermoelastic enhancement of damping of sand using synthetic ground rubber." *J. Geotech. Geoenviron. Eng.* 132 (4): 501–510. https://doi.org/10.1061/(ASCE)1090-0241(2006)132:4(501).

Pouragha, M., N. P. Kruyt, and R. Wan. 2021. "Non-coaxial plastic flow of granular materials through stress probing analysis." *Int. J. Solids Struct.* 222 (Jul): 111015. https://doi.org/10.1016/j.ijsolstr.2021.03.002.

Qi, Y., B. Indraratna, A. Heitor, and J. S. Vinod. 2018. "Effect of rubber crumbs on the cyclic behavior of steel furnace slag and coal wash mixtures." *J. Geotech. Geoenviron. Eng.* 144 (2): 04017107. https://doi.org/10.1061/(ASCE)GT.1943-5606.0001827.

Qian, J.-G., Z.-B. Du, and Z.-Y. Yin. 2018. "Cyclic degradation and non-coaxiality of soft clay subjected to pure rotation of principal stress directions." *Acta Geotech.* 13 (4): 943–959. https://doi.org/10.1007/s11440-017-0567-8.

Sarajpoor, S., A. Kavand, P. Zogh, and A. Ghalandarzadeh. 2020. "Dynamic behavior of sand-rubber mixtures based on hollow cylinder tests." *Constr. Build. Mater.* 251 (Aug): 118948. https://doi.org/10.1016/j.conbuildmat.2020.118948.

Shaverdi, H., M. R. Taha, and F. Kalantary. 2014. "A flow rule incorporating the fabric and non-coaxiality in granular materials." *Granular Matter* 16 (5): 675–685. https://doi.org/10.1007/s10035-014-0525-1.

Symes, M. J. P. R. 1983. "Rotation of principal stresses in sand." Ph.D. thesis, Dept. of Civil Engineering, Univ. of London.

Wang, C., A. Deng, and A. Taheri. 2018. "Three-dimensional discrete element modeling of direct shear test for granular rubber–sand." *Comput. Geotech.* 97 (May): 204–216. https://doi.org/10.1016/j.compgeo.2018.01.014.

Xiong, H., L. Guo, Y. Cai, and Z. Yang. 2016. "Experimental study of drained anisotropy of granular soils involving rotation of principal stress direction." *Eur. J. Environ. Civ. Eng.* 20 (4): 431–454. https://doi.org/10.1080/19648189.2015.1039662.

Yang, Z. X., X. S. Li, and J. Yang. 2007. "Undrained anisotropy and rotational shear in granular soil." *Géotechnique* 57 (4): 371–384. https://doi.org/10.1680/geot.2007.57.4.371.

Yu, H.-S., L.-T. Yang, X. Li, and D. Wanatowski. 2016. "Experimental investigation on the deformation characteristics of granular materials under drained rotational shear." *Geomech. Geoeng.* 11 (1): 47–63. https://doi.org/10.1080/17486025.2015.1006267.